Evaluation of MicroShield Build-Up Factors and their Limits of Applicability

L. Mkhonza

Mini-dissertation submitted in partial fulfillment of the
requirements for the degree of Master of Science in
Nuclear Engineering at the Potchefstroom Campus of
the North-West University

Supervisor: Mr. S. Korochinsky

Co-Supervisor: Prof. E. J. Mulder

Assistance Supervisor: Dr. G. de Beer

November 2007

Abstract

MicroShield is a point-kernel computer code used for gamma-ray shielding and dose rate assessment. It allows the modeling of simple source geometries and simple shielding layouts which lead to very accurate results with low computer time consumption, compared with more advanced methods such as Monte Carlo transport code (e.g., MCNP), among others. The short computer time in finding solutions is due to a deterministic transport using analytic solutions for the direct source contribution (unscattered radiation) to the detector, and then corrected by a build-up factor appropriate for the geometry used in the calculation. On the other hand, Monte Carlo transport codes, such as MCNP, solve the detailed physics of the transport in the real geometry (calculating a build-up factor as a by-product); however, the set up of the geometry and the implementation of variance reduction techniques (always necessary in shielding problems) is complex and time consuming. Although the MicroShield software give good results for many γ-ray shielding and dose rate calculations, there are still many unanswered questions about the behavior of MicroShield build-up factors and their limit of applicability when the line connecting source and detector is not parallel to the normal of the shielding, creating an angle α (offset from symmetry axis). The objective of this work is to compare similar shielding layouts using MicroShield and MCNP, for typical shielding materials and typical energies of interest, but explicitly assessing the incidence of the offset in the results, and therefore determining a limit of applicability for MicroShield. The build-up factors used in the current model of MicroShield have shown to yield reasonable results in terms of the effective dose rates when compared with MCNP calculations at low offset angle. However, as the offset angle increases the results obtained with MicroShield deviates from the MCNP calculations. Using the maximum percentage error of 30 percent as recommended from the MS manual, the limit of applicability of MS was determined at various materials thickness of lead, iron, and concrete.

Declaration

I, the undersigned, hereby declare that the work contained in this project is my own original work.

Signature:..

Date:..21/04/2008..................
Lucky Mkhonza

With the approval of my Supervisors:

Mr. S. Korochinsky
Radiation Safety group (RADS)
PBMR (Pty) Ltd. South Africa

Signature:.......SK...............................

Date:...2008-Apr-21..................

Prof. E. J. Mulder
School of Nuclear Science and Engineering
Potchefstroom Campus of the North-West University

Signature:..

Date:..........................22.04.08

Dr. G. de Beer
Radiation Safety group (RADS)
PBMR (Pty) Ltd. South Africa

Signature:....G A de Beer...

Date:...........21/04/2008..........

Acknowledgements

First and foremost I would like to thank Sergio Korochinsky, Jacek Guzek, and Coenie Stoker for giving me the opportunity to do this work at the Pebble Bed Modular Reactor (Pty) Ltd. I express my indebtedness to my supervisor Sergio Korochinsky for his support, guidance, patience throughout the project. Thanks also to my co-supervisor and assistance supervisor, Prof. E. J. Mulder and Dr. G. de Beer for their helpful contribution towards the success of this work. I would also like to thank Mr. S. Maage and Prof. O. Zamonsky, and all members of the Radiation Safety group (RADS) at PBMR, for helping me to learn the basics of Monte Carlo, and for the many constructive advices and discussions held regarding this work. Not Forgetting Mr. M. Madhuku for his encouraging and support during the two years of my MSc. studies.

This research could not have been accomplished without the financial support from South African Nuclear HUP (SANHARP Program). My warm thanks to Ithemba Labs-Gauteng for allowing me to use their facilities. I thank the School of Nuclear Science and Engineering at the North-West University (NWU-Potchefstroom Campus) for their administration professionalism.

Outside of work I would like to thank my girlfriend and my family for their constant support and encouragement, without which the completion of this work would not have been possible. My father and mother, who passed away, still have deep influence in every aspect of my life. Finally, I would like to give thanks to all my friends, professors, and fellow graduate students for their help and encouragement during my studies.

Contents

Abbreviations

Abbreviation or Acronym	Definition
ANS	American National Standard
ERG	Energy
ICL	Identification of Cell
ICRP	International Commission on Radiological Protection
IPT	Identification of Particle Type
MCNP	Monte Carlo N-particle Transport Code
MeV	Mega Electron Volts
MS	MicroShield
NNR	National Nuclear Regulator (RSA)
PALLAS	Performance Analysis
PBMR (Pty) Ltd	Pebble Bed Modular Reactor (Propriety) Limited
POS	Position
QAD	A Series of Point-Kernel General-Purpose Shielding Programs
RD	Relative Deviation
RSICC	Radiation Safety Information Computational Center
SAR	Safety Analysis Report
TME	Time
2-D	2 Dimensional
3-D	3 Dimensional
WGT	Weight
VRT	Variance Reduction Techniques

List of Tables

List of Figures

1 Introduction

1.1 Background

As part of the licensing process of the Pebble Bed Modular Reactor (PBMR), numerous calculations are performed which are included in the Safety Analysis Report (SAR) that is forwarded to the National Nuclear Regulator (NNR) as part of the application. Many of these calculations are performed with the computer code MicroShield (MS) [1, 2], and the validation and verification of this code is thus required by the NNR.

MicroShield is a point-kernel computer code for photon/gamma-ray (γ) shielding and dose assessment. It is widely used for designing shields, estimating source strength from radiation measurements, minimizing exposure to people, and teaching shielding principles. It is useful to health physicists, waste managers, design engineers, and radiological engineers and only requires a basic knowledge of radiation and shielding principles. MicroShield is fully interactive and utilizes extensive input error checking. Integrated tools provide graphing of results, material and source file creation, source inference with decay (dose-to-Ci calculations accounting for decay and daughter build-up), projection of exposure rate versus time as a result of decay, access to material and nuclide data, and decay heat calculations.

MicroShield allows the modeling of simple source geometries and simple shielding layouts which lead to very accurate results with low computer time consumption, compared with more advanced methods such as Monte Carlo transport code (e.g., MCNP) [3, 4], among others. The short computer time calculations is due to a deterministic transport methodology using analytical solutions for the direct source (unscattered radiation) to the detector, which is then corrected by a build-up factor appropriate for the geometry used in the calculations. On the other hand, Monte Carlo transport codes, such as MCNP, solve the detailed physics of the transport in the real geometry (calculating a build-up factor as a by-product), hence lead to very accurate results, but setting up the geometry and the implementation of variance reduction techniques (always necessary in shielding problems) is complex and time consuming.

Although point-kernel codes give good results for many γ-ray shielding problems for very detailed geometries, there are still many unanswered questions about the behavior of MicroShield build-up factors and their limit of applicability when the line connecting source and detector is not parallel to the normal of the shielding, creating an angle α (offset from symmetry axis) defined by $\alpha = \tan^{-1}(Z/(Q+Y))$ (see Figure 1.1).

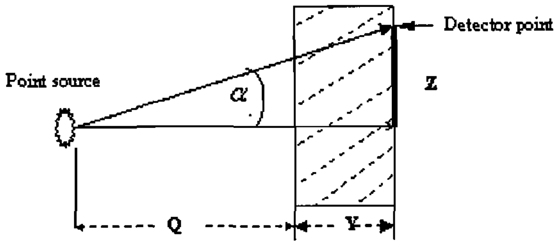

Figure 1.1: Ideal case of an offset angle from symmetry axis

MicroShield validation and verification studies designed for different source geometries to test the offset results as well as symmetry of the results about the axis of the source geometry have been done [5]. However, most of the work performed for MS was only compared to other codes that use similar approximations such as QAD [6, 7]. The MS calculations based on offset from symmetry axis were found to be in good agreement with the QAD results [5].

1.2 Motivation for the Study

As already mentioned in section (1.1), part of the licensing and operating requirements of the PBMR reactor is the physical modeling of the radiation shielding designed for the reactor. The fluxes, and radiation sources at the reactor (which are functions of energy, space, direction and time), are calculated using computer codes such as MicroShield.

It is therefore important that the MS code and the models used are validated and verified according to the requirements from the NNR for the licensing of the PBMR reactor. This work is one of the tasks currently being done by the Radiation Safety group (RADS) at PBMR (Pty) Ltd. In this study the limit of applicability of MS due to an offset angle α assigned to the build-up factors will be obtained by comparing MS results with the reference code MCNP.

The summary of the different materials, parameters and variables chosen for all the case studies are given in Table 1.1.

The most common γ-ray shielding materials used in nuclear reactors and other related facilities are lead, iron, and concrete [8]. Clearly, from Table

Table 1.1: Materials, physical parameters and variables chosen for all the case studies

Material		Lead	Iron	Concrete
	Z	82	26	8-14
Parameters	$\rho[kg/cm^3]$	11.37	7.86	2.35
	Q $[cm]$	2	5	10
	$E\gamma$[MeV]	0.3-3	0.3-3	0.3-3
Variables	$d[cm]$	1-20	2-50	10-250
	α[deg]	0-60	0-60	0-60
μ		High	Medium	Low

1.1, the obvious choice for gamma shielding is lead with $Z = 82$. Lead has the advantage of high atomic number, high density, high linear attenuation coefficient and thus minimizing the volume of material required to reduce the dose due to γ-rays. In addition lead is stable, easily machined, readily available, and is relatively inexpensive, therefore making it an excellent shielding solution.

However, in situations where space is not a constraint and where structural strength is required, concrete is used even though it is a less effective shielding material. As a general shield material, there is much to recommend about concrete; it is strong, inexpensive, and adaptable to both block and monolithic types of construction.

The other material is iron with $Z = 26$. Although it is a medium weight element, it also serves well as a γ-ray attenuator. For γ-rays with energies of 2 MeV, roughly the same mass of iron as of lead is required to remove a specific fraction of the radiation. At higher and lower energies, however, the mass-attenuation efficiency of lead is appreciably greater than that of iron. Selection of iron is also based on its structural, temperature, and economic considerations.

From Table 1.1, the study of each material is characterized by fixed parameters such as material properties (Z, ρ) and geometrical constrains, for example, the distance between source and shield (i.e., Q). Q is defined as 10 % of the maximum thickness of the different material to ensure that a minimum solid angle for Compton scattering is created.

The selected energy range is based on the fact that Compton scattering is the mostly favorable process which contributes towards the photon build-up factors. This energy range is important in providing information about the behavior of the effective dose rate due to the offset angle, hence defining the limit of applicability of MS by comparing with MCNP results.

Since it is important that MS and the radiation shielding calculation models are validated and verified for licensing purposes, the limit of applicability of MS due to build-up factor as a function of an offset angle α will be defined. Also, it is expected that the offset angle will influence the accuracy of the photon flux, and the dose rate through the shielding material. Therefore important information on these parameters and sensitivity of these parameters will be discussed and the limit of applicability of MS will then be determined.

1.3 Research Goals and Objectives

The goal of the proposed work is to define a limit of applicability of MS. This will be achieved by analyzing and comparing the results from MS and MCNP. The objectives of this work are therefore as follows:

- to conduct effective dose equivalent rate simulations based on similar source geometry and shielding layouts using both codes, for typical shielding materials and energies of interest;
- to conduct explicitly the assessment of the incident of the offset in the results; and
- to determine the limit of applicability for MS.

1.4 Outline of Dissertation

The dissertation is presented in six chapters. In chapter 2, the fundamental principles of MS and MCNP codes are given. There is particular emphasis on the various interactions of photons with matter. The point-kernel technique and the photon transport are applicable in MS and MCNP codes, respectively.

Chapter 3 focuses on the model description and set-up used. A description of the geometrical layout of the shielding modeled in MS and MCNP is given. The steps in creating, running, and obtaining output case from the MS code are discussed. Furthermore, the material, source, and tally specifications in MCNP are discussed, together with the implemented variance reduction technique. A short description of the method followed to calculate the effective dose rate is also presented.

Chapter 4 deals with the initial studies of MS. These studies include the investigation of the effective dose rates, build-up factors as well as the interpretation of the results.

In chapter 5, a comparison of the results from MS and MCNP Results is given. This chapter includes, the redefinition of maximum shielding thickness, and the definition of limit of applicability of MS.

The conclusion of this work is presented in chapter 6. This includes recommendations on the limit of applicability that should be implemented when using MS.

2 Fundamental Principles of MicroShield and MCNP

2.1 Interactions of Photons with Matter

When photons pass through a material, some of the photons interact with the particles of the material and the photons can be absorbed or scattered [9, 10, 11, 12, 13, 14]. The absorption and scattering of photons is called attenuation. The number of photons that are attenuated in a medium depends on the number of photons traversing the material, type and density of material. The three main processes through which photons interact with materials are the photoelectric effect, Compton scattering and pair production [9, 10, 11, 12]. Each of these three processes occurs through separate mechanisms at different rates depending on energy and results in varying amounts of energy being transferred to the electrons in the medium. The theory behind the attenuation coefficient as well as the three main photon interactions are provided to generate a clear physical picture of how photons interact with matter.

2.1.1 Linear Attenuation Coefficient

The linear attenuation coefficient (μ) is defined as the fraction of photons that are absorbed or scattered per unit thickness of the absorber material [9, 10, 11, 12, 13]. For example, if A is the number of incident photons, and Δx is the thickness of the absorbing material then the number of photons interacting and being removed from beam, τ, is given by:

$$\tau = \mu A \Delta x. \tag{2.1}$$

Now, let ΔA be the change in the number of photons in the beam in passing through Δx. Since A is reduced by one for each interaction (i.e., $\Delta A = -\tau$), equation 2.1 can be written as follows:

$$\Delta A = -\mu A \Delta x, \tag{2.2}$$

Equation 2.1 describes how A changes as photons pass through the attenuator, whereas Equation 2.2 gives the number of interactions in a slab of thickness Δx bombarded by a beam of A photons. The attenuation produced by thickness Δx will depend on the type of target (e.g., number of electrons, atoms, or nuclei) present in the layer. If a layer were to be compressed to half the thickness, it would still have the same number of electrons and the photons will still be attenuated by the same fraction; however, its attenuation coefficient would be two.

If cross-sections σ_{pe}, σ_c and σ_{pp} are assigned to the photoelectric effect, Compton scattering and pair production, respectively, then linear attenuation coefficient for removal of photons from a homogeneous beam may be written as

$$\mu = N(\sigma_{pe} + \sigma_{pp}) + ZN\sigma_C, \tag{2.3}$$

where N is the number of atoms of absorber per cm^3. The atomic number Z multiplies the cross-section, σ_c, because the Compton effect takes place with individual electrons rather than with atoms as a whole. This is in fact true only when the momentum transferred to an electron in the incoherent scattering process considerably exceeds $\sqrt{2m_eE_b}$, where E_b is the electron binding energy, so that the electron may be treated as free. If this is not so the Compton scattering cross-section per atom, $Z\sigma_C$ is reduced [13]. The mass attenuation coefficient, μ_m is obtained by dividing μ by the density of a particular absorber. Figure 2.1 shows the variation of μ_m with energy for lead. Clearly the energy is not a single-valued function of μ_m because the pair production cross-section increases with energy while the photoelectric and Compton cross-sections decrease. The relative importance of these three main processes as a function of energy and atomic number of absorber is shown in Figure 2.2. Measurements of the attenuation coefficient near minimum absorption is therefore not an unambiguous method of determining photon energy in this region of the spectrum.

2.1.2 Photoelectric Effect

In the photoelectric absorption process, an energetic photon interacts with an orbital electron of an atom, followed by subsequent ejection of the electron

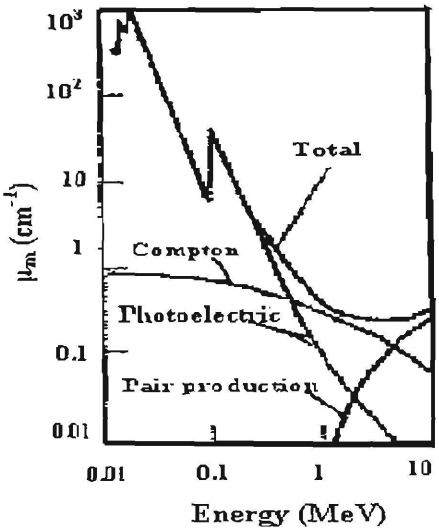

Figure 2.1: Mass attenuation coefficient for γ-rays in lead ($Z = 82, \rho = 11.3\,g/cm^3$).

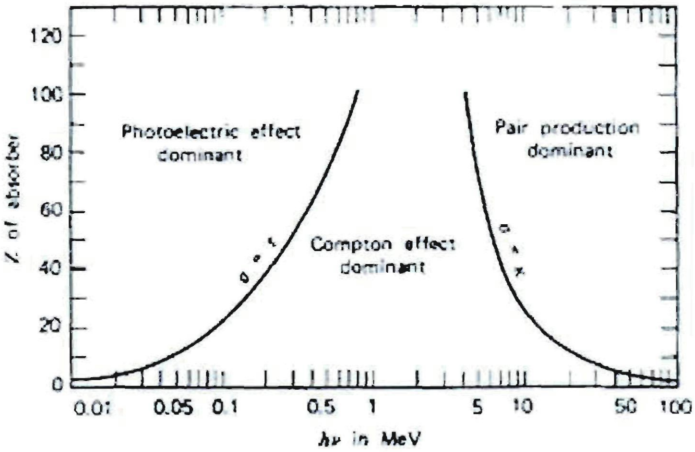

Figure 2.2: The relative importance of the three major types of γ-ray interaction.

from the atom (see Figure 2.3):

$$\gamma + atom \rightarrow atom^{+} + e^{+} \tag{2.4}$$

The interaction is with the atom as a whole and it does not take place with free electrons. For γ-rays of sufficient energy, the most probable origin of photoelectron is from the mostly tight bound or K-shell of the atom [10]. The photoelectron appears with an energy, E_e given by

$$E_e = E_\gamma - E_b, \tag{2.5}$$

where $E_\gamma = hv$ is the photon energy and E_b is the electron binding energy [10, 15]. The photoelectric effect is more likely to occur when the photon energy is less than 0.5 MeV.

During photoelectric effect, the ejected photoelectron leaves a vacancy in the atomic electron structure, and a cascade of characteristic x-rays is produced as the remaining atomic electrons are rearranged to fill the vacancy. Occasionally such an x-ray may interact with and eject a less tightly bound outer electron (Auger electron) with energy equal to that of the x-ray minus the binding energy of the outer electron. Figure 2.3 shows the process of the photoelectric effect.

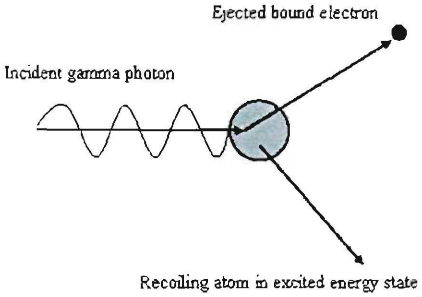

Figure 2.3: Ejection of a bound electron by a γ-ray: The photoelectric effect.

The photoelectric absorption process is the predominate mode of interaction for γ-rays or relatively low energy (< 0.5 MeV). The process is also enhanced for absorber materials of high atomic number Z. No single analytic expression is valid for the probability of photoelectric absorption per atom over all ranges of E_γ and Z, but a rough approximate expression for the probability is

$$\sigma_{\tau} \cong constant \times \frac{Z^n}{E_{\gamma}^{3.5}} = \frac{\mu_{pe}}{N}, \tag{2.6}$$

where N is the number of atoms of absorber per cm^3, μ_{pe} is the photoelectric effect linear attenuation coefficient. The exponent, n, varies between 4 and 5 over the γ-ray energy region of interest [16, 17]. This dependence of the photoelectric absorption probability on the atomic number of the absorber is a primary reason for the preponderance of high-Z materials (such as lead) in γ-ray shields. Equation 2.6 indicates that $\mu_{pe} \propto Z^5/E_{\gamma}^{3.5}$, and this implies that the photoelectric linear attenuation coefficient is large for elements of high atomic number, and increases with decreasing γ-ray energy as shown in Figure 2.1.

2.1.3 Compton Scattering

In Compton scattering, a photon collides with a loosely bound outer shell orbital electron of an atom, loses some of its energy and is deflected from its original direction of travel (see Figure 2.4). The relation between the deflected photon and the energy loss for Compton scattering, assuming the electron to be free and at rest, is determined from the conservation of momentum and energy between the photon and the recoiling electron [10, 12, 13, 16, 17]. This relation can be expressed as

$$E_{\gamma}^{'} = \frac{E_{\gamma}}{1 + (E_{\gamma}/E_e)(1 - cos\theta)}, \tag{2.7}$$

where E_{γ} is the initial energy of the photon before scattering and $E_e^{'}$ is the final energy of the photon after scattering, $E_e = m_e C^2$ is the total energy of the electron at rest, and θ is the photon deflection angle.

The probability of Compton scattering per atom of the absorber depends on the number of electrons available as scattering targets and therefore increases linearly with Z. The variation of γ-ray energy with the Compton linear attenuation coefficient, $\mu_c \propto Z/hv$ is indicated in Figure 2.1 for lead and μ_c decreases with increasing γ-ray energy.

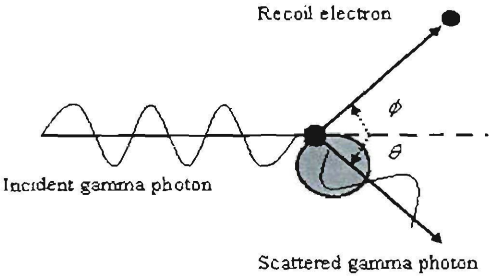

Figure 2.4: Scattering of a γ-ray by a free electron: Compton scattering.

The basic theory of Compton scattering, is well described by Klein and Nishina [18] and experimentally confirmed by references [19, 20]. The angular distribution of scattered γ-rays is predicted by the *Klein – Nishina Formula* for the differential scattering cross section $d\sigma/d\Omega$ [10, 16]

$$\frac{d\sigma}{d\Omega} = Zr_0^2 \left[\frac{1}{1+\alpha(1-cos\theta)}\right]^2 \left[\frac{1+cos^2\theta}{2}\right] \left[1+\frac{\alpha^2(1-cos\theta)^2}{(1+cos^2\theta)[1+\alpha(1-cos\theta)]}\right], \tag{2.8}$$

where $\alpha \equiv hv/m_0C^2$ and r_0 is the classical electron radius.

2.1.4 Pair Production

In pair production, photons with energy greater than 1.022 MeV interact in the vicinity of the coulomb field with a nucleus; the γ-ray disappears and is replaced by an electron-positron pair (see Figure 2.5). All the excess energy carried in by the photon above the 1.022 MeV required to create the pair goes into the kinetic energy shared by the positron and the electron (i.e., 0.511 MeV each). The excess energy will be carried away equally by these two particles which produce ionization as they travel in the material. The positron is eventually captured by an electron and annihilation of the two particles occurs. This results in the release of two photons each of 0.511 MeV known as annihilation radiation [10, 13, 16, 17]. These two photons then lose energy by Compton scattering or photoelectric effect.

The magnitude of the probability of pair production per nucleus varies approximately as the square of the absorber atomic number (i.e. $\sigma_n \propto Z^2$).

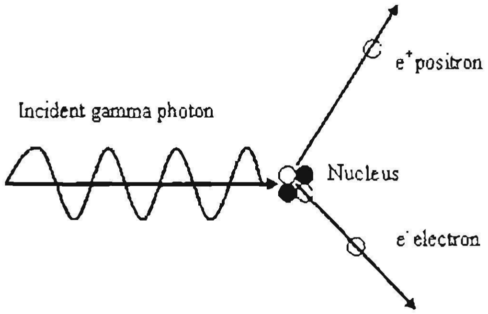

Figure 2.5: The process of pair production.

The variation of pair production mass attenuation coefficient increases with increasing γ-ray energy as shown in Figure 2.1.

2.1.5 Photon Build-Up Factor Concept

As already mentioned in section 2.1, a beam of photons passing through different materials can either be absorbed or scattered. In addition, some of the photons can travel trough the medium without any collision. For a narrow beam of mono-energetic photons of γ-rays (see Figure 2.6), the photon fluence rate (flux) or the intensity which passes through a material without any collision, ϕ_u can be expressed as [9, 21, 11]:

$$\phi_u = \phi_0 e^{-\mu d}, \tag{2.9}$$

where ϕ_0 is the flux of initial photons, μ is the linear attenuation coefficient in cm^{-1} and d the thickness of material in cm.

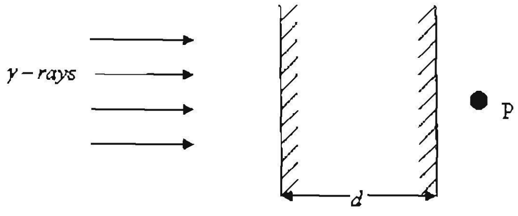

Figure 2.6: Narrow beam of rays incident on slab shield.

The exponential absorption described in equation 2.9 is useful for calculating the flux for narrow beam source geometry. However, this equation underestimates the required shield thickness for broad beam source geometry or for thick shields because it assumes that every photon that interacts with the shield is removed from the beam, and thus does not contribute to the flux.

For a broad beam source or thick shield, the total photon fluence flux, ϕ_T at some point of interest r is the sum of two components: the uncollided fluence, ϕ_u of photons that have streamed to r directly from the source without interaction, and the scattered or secondary photon fluence, ϕ_s consisting of source photons scattered once or more, as well as secondary photons such annihilation γ-rays (see Figure 2.7). The total fluence can be written as

$$\phi_T = \phi_u + \phi_s. \tag{2.10}$$

Thus, in practice, the absorption Equation 2.9 is modified by introducing the build-up factor B such that:

$$\phi_T = B\phi_0 e^{-\mu d}. \tag{2.11}$$

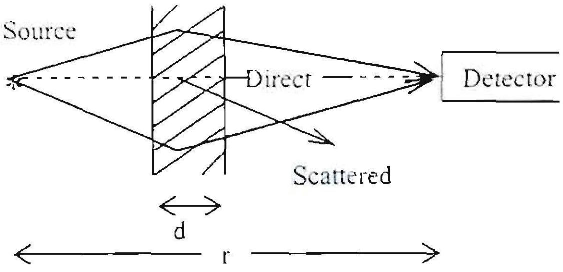

Figure 2.7: Schematic diagram illustrating the photon scattering concept.

For an isotropic point source (as shown in Figure 2.7) in infinite homogeneous media, the total flux of photons becomes:

$$\phi_T = \frac{S_0 B}{4\pi r^2} e^{-\mu d}, \tag{2.12}$$

where S_0 is the source strength. Equation 2.12 can also be written in terms of the total dose absorption rate by incorporating the detector response function, $\mathscr{R}$ (fluence-to-dose-rate conversion factor), and it becomes

$$D_T = \frac{S_0 B \mathscr{R}}{4\pi r^2} e^{-\mu d}. \tag{2.13}$$

The build-up factor, B is defined as the ratio of the total dose, D_T (scattered dose D_s plus un-collided dose D_u) to the dose of un-collided photons only [9, 21, 2, 22]

$$B = \frac{D_T}{D_u} = 1 + \frac{D_s}{D_u}, \tag{2.14}$$

Build-up factors are not constant, but rather vary with a number of parameters such as medium thickness, geometry, source energy, and detector position (affected by offset from symmetry axis) [21].

The γ-ray build-up factors for isotropic point source in infinite homogeneous media have been widely used in γ-ray shielding calculations combined with the point-kernel model. There are many software codes which are based on the point-kernel model. Some that have been widely used or in use today can be found in references [1, 23, 24, 25, 26]. The earliest data set of γ-ray build-up factors was developed by Goldstein and Wilkins [27] based on the moments method and accounted for Compton scattering photons. The comprehensive data set of build-up factors was further developed by the American Nuclear Society [28]. The relevant data were obtained based both on the moments method calculations for low-Z elements and on the calculations using the PALLAS code [29] for high-Z elements up to several depths of mean free paths. This data serves as a reference for all shielding radiation calculations based on the point-kernel model.

The use of build-up factors in shielding design and analysis is greatly facilitated by interpolation methods devised by Taylor, Berger and Capo [30, 31, 32]. For an isotropic point source in an infinite medium, these interpolation formulae are given by

$$B_m(E_\gamma, \lambda) \approx Ae^{-\alpha_1\lambda} + (1-A)e^{-\alpha_2\lambda}, \tag{2.15}$$

$$B_m(E_\gamma, \lambda) \approx 1 + C\lambda e^{D\lambda}, \tag{2.16}$$

and

$$B_m(E_\gamma, \lambda) \approx \sum_{n=0}^{3} \beta_n \lambda, \tag{2.17}$$

where λ is the number of mean free paths at source energy. Parameters A, α_1, α_2, C, D, and β_n depend on the material, the photon energy, and, in principle, the nature of the response.

2.2 MicroShield Code

2.2.1 Introduction to Microshield Code

As already mentioned in the introduction MS is a γ-ray shielding and dose assessment program that is widely used for designing shields, estimating source strength from radiation measurements, minimizing exposure to people, and teaching shielding principles [1]. MicroShield is fully interactive and utilizes extensive input error checking. Integrated tools provide graphing of results, material and source file creation, source inference with decay (dose-to-Ci calculations accounting for decay and daughter build-up), projection of exposure rate versus time as a result of decay, access to material and nuclide data, and decay heat calculations.

The most important features describing the capability of MicroShield include:

- Sixteen geometries that accommodate offset dose points and as many as ten standard shields plus source self-shielding and cylinder cladding.

- The geometry display for entry is re-scaled as dimensions are entered. Dimensional data are accepted in meters, centimeters, feet, or inches. Display can be rotated in 3-D for viewing and printing.

- Library data (radionuclides, attenuation, build-up, and dose conversion) reflecting standard data from RSICC, ANS, and ICRP.

- Provides the ability to access and use the optional ICRP-38 Nuclide Library. This library, which is significantly larger than the standard library, is currently being distributed with RadDecay 2.0. Microshield will keep track of which library is used during the analysis or the creation of a source file.

- Build-up and uncollided results are both automatically and simultaneously calculated.

- Sources may be created, saved and moved among cases, either as nuclides or energies, or as concentrations or totals. Several photon grouping methods are provided including custom (user defined).

- Source decay can be calculated with daughter products generated.

- Provides the ability to design and save up to eight custom materials for any case to add to the twelve built-in materials.

- As many as twenty-five energy groups (with an energy range of 15 keV to 10 MeV) may be used; input may be concentration or totals.

- Sensitivity of exposure rate to time, source dimension, shield thickness, or distance can be investigated. Integration conversion verification can be conducted with sensitivity to quadrature order.

- Decay heat/energy can be calculated.

- Improved flexibility for users to control input and output units, case file saving, printing, and emailing, export of results including graphs to office documents.

- Provides the ability to define multiple (up to six) dose points for a case for almost all geometries.

- Provides the ability to operate on multiple cases simultaneously.

- Improved handling of graphics including displayed and printed graphs as well as the case model.

The fundamental theory of MS is based on a point-kernel model/technique with idealized geometry. The following section will briefly explain this technique to generate a clear picture of MicroShield principles.

2.2.2 Point-Kernel Technique

In most practical shields designed to attenuate penetrating radiation (e.g., photons) in nuclear reactors, extended sources are considered [9, 8]. All extended sources are considered to be composed of differential isotropic point sources. Point sources are those sources in which the variation of radiation particle flux density, ϕ with distance, r is described by the following expression:

$$\phi = B\frac{S_0}{4\pi r^2}e^{-\mu x}, \tag{2.18}$$

where B is the build-up factor, S_0 is the source strength, μ absorption coefficient, and x is the thickness of the absorbing material.

The response (e.g., dose rate) of a detector due to any extended source may be obtained by summing or integrating the responses from the point sources from which the extended source is made up. Let us consider a volume element dV as a point-kernel of a mono-energetic isotropic volume source with source strength $S_V(\mathbf{r}_s)$ placed at position $\mathbf{r}_s$ and the isotropic point detector (a target) is placed at $\mathbf{r}_x$ in a homogeneous medium. The total dose rate can be expressed as,

$$D(\mathbf{r}_s) = \int_V \frac{\mathscr{R}S_V(\mathbf{r}_s, E)B(\mu, E)}{4\pi r^2}e^{-\mu x}dV, \tag{2.19}$$

where $\mathscr{R}$ is the flux-to-dose conversion factor, $B(\mu, E)$ is the dose build-up factor, $\mu(E)$ is the linear attenuation coefficient, and $r = |\mathbf{r}_s - \mathbf{r}_x|$ is the source to detector distance.

Equation 2.19 holds for any geometry or medium provided that the material through which a ray from $\mathbf{r}_s$ to $\mathbf{r}_x$ passes has a constant interaction coefficient $\mu(E)$. If the medium is heterogeneous (see Figure 2.8) between $\mathbf{r}_s$ and $\mathbf{r}_x$, then, in the expression above, $exp(\mu x)$ is replaced by $exp(l)$, where l is the distance in mean-free-path length between $\mathbf{r}_s$ and $\mathbf{r}_x$, and is expressed as

$$l = \int_0^r \mu(s)ds. \tag{2.20}$$

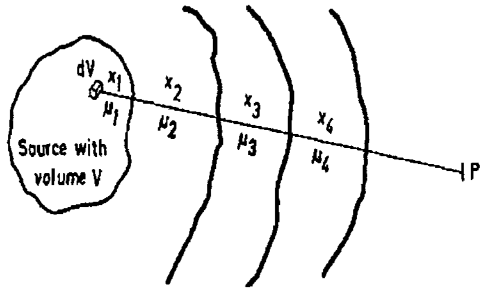

Figure 2.8: Ideal case representing a volume source

From equation 2.19 it can be seen that the total dose at $\mathbf{r}_x$ from an isotropic volume source depends on the material properties along a line joining $\mathbf{r}_s$ and $\mathbf{r}_x$ and on the distance between these two points. This approximation is based on build-up factors, is sometimes called *ray theory*, indicating that the total dose is determined simply by the material and distance along the ray joining source and detector points [9, 8]. In many situations it is an excellent approximation and is widely used in photon shielding calculations.

2.3 MCNP Code

MCNP is a general-purpose Monte-Carlo N-particle code that can be used for neutron, photon, electron, or coupled neutron/photon/electron transport, including the capability to calculate eigenvalues for critical systems [3, 4]. It treats an arbitrary three-dimensional configuration of materials in geometric cells bounded by first- and second-degree surfaces and some fourth-degree surfaces, and uses point wise (continuous) cross-section data with photon energy ranging from 1 keV to 100 GeV, for electrons ranging from 1 keV to 1 GeV, and for neutrons ranging from 10-11 eV to 20 MeV.

MCNP is a stochastic process involving a randomly determined sequence (using random numbers) of observations each of which is considered as a sample of one element from a probability distribution, analogous to throwing dice in a casino, hence the name Monte Carlo [3, 4, 33, 34].

MCNP is among the first physics codes produced and became available on any commercially viable, state-of-the-art computers. It has been made as system independent as possible to enhance its portability, and has been written to comply with the ANSI-Standard FORTRAN 90 and global data is shared via FORTRAN modules [3, 4].

2.3.1 Photon Transport in MCNP

In particle transport, the Monte Carlo technique is pre-eminently realistic. It follows each of many particles from a source throughout its life to its death in some terminal category (e.g. absorption, escape, etc). The outcome at each step of its life is randomly sampled from probability distribution using transport data. Figure 2.9 is an example of a photon history in Monte Carlo transport theory.

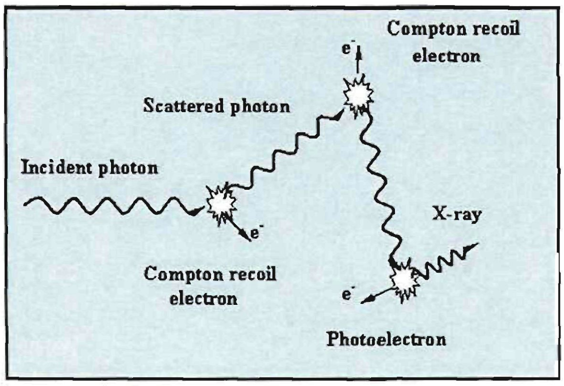

Figure 2.9: Photon history in Monte Carlo method.

When following a photon, MCNP starts to verify if it interacts or not in a medium. The probability that a photon will travel a distance S without undergoing any interaction is given by $exp\left(\Sigma_T S\right)$, where $\Sigma_T S$ is the probability to interact in the interval dS. So, the probability for a first collision to occur between S and $S + dS$ along its line of flight is

$$P(S)dS = e^{\Sigma_T S}\Sigma_T dS, \tag{2.21}$$

where Σ_T is the macroscopic total cross-section of the medium and is interpreted as the probability per unit length of a collision. Setting ξ to be a random number which is uniformly distributed on interval (0.1), with the line of flight to l, to be

$$\xi = \int_0^l P(S)dS = 1 - e^{\Sigma_T l}, \tag{2.22}$$

this can be expressed as:

$$l = -\frac{1}{\Sigma_T} ln(1 - \xi), \tag{2.23}$$

but, because $1-\xi$ is distributed in the same manner as ξ, the equation can be rewritten and an expression for the distance to the first collision is obtained as

$$l = -\frac{1}{\Sigma_T} ln(\xi). \tag{2.24}$$

The photon is then transported to the location of the first interaction (collision). Subsequently, the type of interaction to be simulated is sampled, based on the partial cross-section for different interactions contained in the interaction data tables [3, 4, 35]. The theories describing the kinematics of the various photon interactions are implemented during the photon transport. For example, in the Compton scattering, the energy and direction of the scattered photons are sampled. The process is repeated until the photon is absorbed or escapes from the system.

2.3.2 Input and Output for MCNP

Before running a simulation in MCNP the user creates an input file, in which the problem to be simulated is defined. The contents of the input file for MCNP are presented as follows:

Problem Title Card
Cells Cards

Surface Cards

Data Cards

The first row is a title card which contains information describing the problem to be simulated. The cells specification cards define the geometric volumes, which together make up the model set-up that will be used in the simulation. The cell cards contain information about the geometry, the user's specified materials with their respective densities. They also contain information about the particle type with a specific importance in each cell. The surface cards define all surfaces in terms of position and shape. The surface cards are invisible and contain no material and they are used to define the shape of the cells.

The Data cards contain most of the information about the whole simulation model, except for the geometry. For example, the necessary information includes the source specification, particle type, particle energy, the number of events, the material composition, variance reduction techniques and how and what type of answer is desired, etc. The type of answer desired by the user is obtained by using the scoring process (i.e., tallies). Tallies are determined by a variety of estimators which evaluate fluence, or fluence like-quantities, at a point or region. The most frequently used tallies are current at a surface (F1), average flux at a surface (F2), flux at a point or ring (F5), and average flux over a cell (F4). Similar to flux tallies over a cell are various tallies of energy deposition (F6 and F7).

The quality of MCNP results can be evaluated with the relative error presented in the output file. The relative error, is defined as:

$$RE = \frac{C}{\sqrt{N}}, \tag{2.25}$$

where N is the number of samples (particle histories) and $C = \sigma_x/\overline{x}$ is the relative error in population of samples, where σ_x is the variance and $\overline{x}$ is mean value. For a generally reliable result, RE should not be larger than 0.1. If the error is large MCNP will print a warning in the output file.

The efficiency of the simulation can also be evaluated from the figure of merit (FOM), which is defined as:

$$FOM = \frac{1}{RE^2 T}, \tag{2.26}$$

where T is the computer time in minutes. The more efficient the Monte Carlo calculation is, the larger the FOM will be because less computer time is required to reach a given value of RE [3].

3 Model Description and Set-Up

The work in this thesis has mainly been done with the help of two computer codes. MicroShield has been used to simulate the effective dose rates with respect to the offset angle and MCNP has been used for comparison.
In this chapter, the description of the model with MS and MCNP as well as the strategy in calculating the dose rate points are explained.

3.1 MicroShield Model Description

The geometrical source configurations modeled with MS include: point, line, disk, rectangular area - vertical and horizontal, sphere, cylinder volume - side shields, cylinder volume - end shields, cylinder surface - internal and external dose point, annular cylinder - internal and external dose point, rectangular volume, truncated cone, infinite plane, and infinite slab.

The geometrical layout of the model as defined in the MicroShield code will be described in the next section.

3.1.1 Geometry Layout of MicroShield

The geometry layout modeled for this work includes the distance and orientation between the source, dose point as well as the intervening shields.

For the purpose of this work, a simple geometry with an isotropic point source and a slab shield material of air, lead, iron, and concrete were modeled. Figure 3.1 is a 3-D schematic diagram as modeled in the MS code for different possible dimensions for all shielding materials (i.e., concrete, lead, and iron). The point source is positioned at the origin of the x, y, z coordinate system (MS does this by default). The first slab shield material on the left represents air. The first slab shield material was chosen to be air to avoid a contact of the source with the slab shield of lead, iron, or concrete. In addition, in most practical cases in nuclear engineering, in the shielding of gammas or neutrons a gap is always available to permit the flowing of the cooling system. The second slab represents the shielding material to be used during the run. The six dotted points represents the dose rate points.

3.1.2 Creating a Case

To create a case study for each material, the point geometry setup as explained above was chosen from the new file menu of the MS interface. The

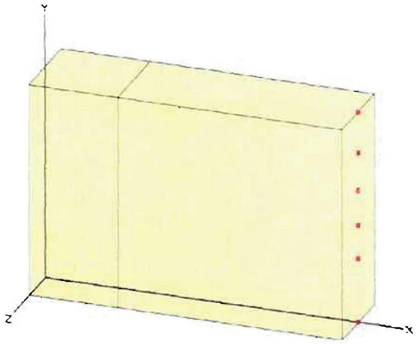

Figure 3.1: 3-D view of geometrical layout as modeled in MicroShield.

input steps for a new case were constrained by fixed sequence as recommended in the MS manual. For modifying an already defined case, the steps below may be exercised in parallel since there already exists a basis for other input steps.

- The first step in designing a case is to assign the dimensions of the source, shields, and dose point locations which give the physical layout shown in Figure 3.1.

- The second step is to assign the material densities for the slab shield of air, lead (or iron or concrete), as well as the air gap between the shielding material and the source points. Material information is required for build-up factor reference material prompting.

- The third step is to assign the source strength. For the purpose of this work the user defined method for the photon energy was considered. This method allowed us to enter photon energies ranging from 0.3 - 3 MeV and the activity of $1Ci = 3.7 \times 10^{10}$ in photons per second for each value of energy. Photon energies are required for build-up factor reference material prompting.

- The fourth step is to assign the build-up factor reference material which in this study is lead, iron, and concrete. Build-up factors are retrieved and interpolated from tables of data.

- The fifth step in creating the case is to assign the integration parameters (depending on the geometry of the case). In this study this step was not required because an isotropic point source was considered.

- The sixth step is to give the case a title and description, for user convenience.
- The last step is the sensitivity analysis - this step allows the user to evaluate sensitivity of exposure to user selected variables. It was not necessary to go through this last step because it is not part of the proposed work. However, it could be used to perform a further validation step if necessary.

3.1.3 Running a Case

To explain the steps in running the case in MS a single run is considered (a batch run can also be created in MS). After creating the case geometry as explained in section 3.1.2 the next step is to run it. Upon initiation of the executation of a single case, MS does the following:

- formulates the linear attenuation coefficients for each shield based on the densities and material designated. MicroShield looks up values for mass attenuation coefficients by material type and bracketing energies, interpolates for energy, multiplies by the individual material density, and sums to obtain linear attenuation coefficients for each shield region. The linear attenuation coefficients are multiplied by the physical path length through each shield and then summed over all shields.
- uses the reference build-up factor material for each case energy to create arrays of build-up factor times attenuation factor with mean free paths as the independent variable.
- for each kernel (in case of a volume source) and for each case energy, mean free paths are determined between the kernel and the dose point through the intervening materials.
- the uncollided and build-up photon fluence rate are both calculated at the dose point for each kernel and added to results for previous kernels.
- Steps 3 and 4 are repeated for each dose point.

3.1.4 Case Output

The fundamental result of point-kernel integration is the photon fluence rate ($photons/cm^2/sec$) at the dose point in the case. This is multiplied by energy to achieve the energy fluence rate, ($MeV/cm^2/sec$). To provide usable results, photon fluence rate is converted to units of exposure, energy absorption in air, and the effective dose equivalent (important in this study). These use conversion tables in ICRP publication [36], and the units definitions of the Sievert, among others.

Automatic conversions is conducted to exposure rate in air, expressed as milli-Sievert per hour (mSv/hr). The exposure rate in air is determined using table 11 in reference [36]. This table was calculated with values of mass energy absorption coefficients for dry air by reference [15]. MicroShield V6.02 simultaneously calculates the uncollided fluence rate (without build-up) and the effects of scatter (with build-up).

3.2 MCNP Model Description

The MCNP input file is an ASCII file containing command lines called cards (cell cards, surface cards, and data cards). The cards provide a description of the situation that is to be simulated, such as:

- the geometry specification,
- the material specification and cross-section selection,
- the location and the characteristics of the neutron, photon, or electron source,
- the type of answer desired, and
- any variance reduction techniques (chosen by the user) used to improve efficiency.

To explain how the geometry layout of the model was constructed using the different cards as mentioned above the input file of MCNP given in appendix A.1 was considered.

3.2.1 Geometry Layout of MCNP

The geometry defined in the input file of MCNP is treated by three-dimensional configuration of user-defined materials in cells bounded by regions called surfaces. The cells are treated in a Cartesian coordinate system and are formed by intersections, unions, and complements of regions bounded by surfaces. When the cells bounded by surfaces are defined correctly in the cell cards, MCNP will track the particle path by checking the sense of the intersection point for each surface listed for the cell.

The geometrical layout modeled for this work using MCNP is shown in Figure 3.2. The source and shield are surrounded by a sphere outside of which particle transport is terminated. In MCNP terminology, the exterior of this sphere is referred to as the outside world. The tori for tallies are indicated on the right side of the shield. The vertical black line shown in middle of the shielding material indicates the splitting of the slab for variation reduction technique (i.e., splitting).

The geometry layout modeled with MCNP was designed in such a way that it represents the actual MicroShield setup as closely as possible. In the case of tally F4, a small gap of 0.0001 *cm* between the shielding material and detector was provided to avoid a geometrical error in MCNP run.

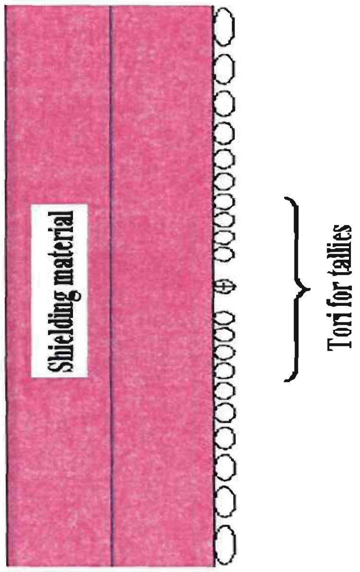

Figure 3.2: 2-D Vertical cross-section of geometrical layout as modeled in MCNP.

The first line numbered 1 in the input file (Appendix A.1) is the title card describing the problem to be run. The next line numbered 2 beginning with c is a comment line and it representing the beginning of the geometry cells. The first column in line number 3 represents the cell numbered 1, and the next column after the cell numbered 1 column represents the cell material number (lead/concrete/iron in this work), followed by the 3^{rd} column representing the cell material density (it is entered as negative entry which is interpreted as mass density in units of g/cm^3).

The subsequent numbers after each cell material density entry represent a complete specification of the geometry of the cells that follows. This specification includes a list of surfaces bounding the cell where the signs indicate the sense of the regions defined by the surfaces. In this case, cell 1 with specific cell material density for concrete is bounded by 6 surfaces, and has an importance of one. Lines numbered 22 to 27 are the repetition of the above description for different cell numbers with different importances. In cell card numbered 2, the cell material density is considered as void because there is no material and this cell represents the vacuum of the system and it is bounded by 19 surfaces and it has an importance of one. Lines 8 to 19, represents cell cards for different tallies with no material and bounded by different surfaces but similar importances. Line 31 which is a void cell, represents the boundary for the system (outside world), it is bounded by only one surface numbered 7, and has an importance of zero (any particle crossing this boundary is terminated).

Line 33 represents the comment line describing the starting point for surface cards. The next line numbered 34 starts with a surface number 1, followed by an alphabetic mnemonic indicating the surface type. In line 34, surface 1 (PZ 3000) is a plane normal to the z-axis. This description is similar for surfaces 2-6 (in lines 35-39) as well as 22-27 (in lines 54-59) for the remaining axis. In line 40, surface 7 (SO 6020) is a sphere with radius 6020 cm from the origin. In line 41, surface 8 is an ellipsoid which is located at (0, 5.0501, and 0) coordinate along the y-axis with minor and major radius of 0.227533 and 420 cm, respectively. Line 42, surface 11 is a torus, the first 3 entries after the alphabetic mnemonic indicates the origin of the torus (i.e., x,y,z-coordinates), the 4th, 5th and 6th entries represents the major (i.e., inner radius of the torus itself), thickness and minor radius of the torus (i.e., the radius of the cross-section of the torus). Similarly for surfaces 12-21 in lines 43-52 for different dimensions.

3.2.2 Material Specification

The material specification card specifies both the elemental (or isotopic) composition of materials and the cross-section evaluations to be used in the cells. This card is used to specify a material for all cells containing material m, where m cannot exceed more than five digits:

$Mm \quad ZAID_1 \ fraction_1 \ ZAID_2 \ fraction_2$......

The m corresponds to the material number on the cells cards. The consecutive pairs of entries in the material card consist of the identification number ($ZAID$) of the constituent element or nuclide followed by atomic fraction (or weight fraction if entered as a negative number) of that element or nuclide, until all the elements and nuclides needed to define the material have been listed.

The nuclide identification number ($ZAID$) is used to identify the element or nuclide desired, and the form of the number is $ZZZAAA.nnX$, where:

- ZZZ is the atomic number of the element or nuclide,
- AAA is the mass number of the nuclide, ignored for photons and electrons,
- nn is the cross-section evaluation identifier. If blank or zero, a default cross-section evaluation will be used, and
- X is the class of data: C is continuous energy; D is discrete reaction; T is thermal; Y is dosimetry; P is photon (relevant in this study); E is electron; and M is multigroup.

For naturally occurring elements, $AAA = 000$. Thus $ZAID = 82000$ represents lead, and $ZAID = 26000$ represents the element iron.

The material specification in this work is provided in appendix A.1. Line 63, $m1$ corresponds to the material number on the cell card. The remaining pairs of entries after this number consist of the identification number ($ZAID$) representing the constituent elements for concrete followed by the weight fraction of that specific element and this sequence is continued until all the elements constituting the material concrete have been listed.

3.2.3 Source Specification

The source and type of radiation for MCNP are specified by the SDEF command. The SDEF command has many variables or parameters that are used to define all the characteristics of all sources in the problem. The SDEF command with many variables is one of the more complex MCNP commands and is capable of producing an incredible variety of sources-all with a single SDEF command. Some of the sources are point source, area source, volume source and multiple sources. Only one SDEF card is allowed in an input file.

The source has to define the values of the following MCNP variables for each particle it produces: ERG-the energy of the particle (MeV), TME-the time when the particle started (shakes), POS-the position of the particle, IPT-the type of the particle, WGT-the statistical weight of the particle, ICL-the cell where the particle started, and JSU-the surface where the particle started or zero if the starting point is not on any surface.

The source specification used here is defined in line 84 indicating the particle: source energy (ERG), the statistical starting weight (WGT), and the position of the source (POS). The definition of starting cell (CEL) and the starting direction for source particles in this work is not included in the input file because for an isotropic source MCNP determine the above parameters by default.

3.2.4 Tally Specification

The tally (scoring) cards in the MCNP input file are used to specify the parameters of interest, that is, type of answers from the Monte Carlo calculation. The scoring process is determined by a variety of estimators which evaluate fluence, or fluence like-quantities, at a point or region. The most frequently used tallies are current at a surface (F1), average flux at a surface (F2), flux at a point or ring (F5), and average flux over a cell (F4). Similar to flux tallies over a cell are various tallies of energy deposition (F6 and F7). For the purpose of this work, tally F4 and F5 were used to obtain information about the effective dose rate in a cell and at a point.

The physical significance of tally F4 can be well understood by considering a particle of weight, W and energy, E which makes a track-length (segment) T within a specified cell of volume, V. This segment makes a contribution WT/V to the flux in the cell. The sum of the contributions is reported as the F4 tally in the MCNP output. Technically, if $\phi(\mathbf{r}, E, \Omega)$ were the energy and angular distribution of the fluency as a function of position, the F4 tally would measure

$$^{*}F4 = \frac{1}{V}\int_V dV \int_E dE \int_{4\pi} d\Omega \mathscr{R}(E)\Phi(\mathbf{r}, E, \Omega), \tag{3.1}$$

where $\mathscr{R}(E)$ is a fluence-to-dose conversion factor. MCNP will carry out this calculation, obtaining values of $\mathscr{R}(E)$ by interpolation of values specified in a table placed in the input file (lines 116 - 140-appendix A.1). The form of the table is

$DE4\ A\ E1\ E2 \ldots Ek\ , \$ energy\, grid\, for\, fluence - to - dose\, factors$

$DF4\ B\ F1\ F2 \ldots Fk\ \$ fluence - to - dose\, conversion\, factors$

Entries $E1$ through Ek are tabulated values of energy and $F1$ through Fk are corresponding tabulated values of $\mathscr{R}(E)$. Entries A and B, either LOG or LIN, specify logarithmic or linear interpolation, respectively.

Unlike F4, F5 does not require a particle to reach the detection location. F5 scores at every collision the probability that the next event being at the detector side, and scores $Wp(\mu)exp(-\lambda)/r\pi r^2$. Where $p(\mu)$ is the value of the probability density function at μ, the cosine of the angle between the particle trajectory and the direction of the detector, λ the total number of the mean-free-paths integrated over the trajectory from the collision point to the detector and r is the distance between the collision point and the detector. The probability density function, $p(\mu)$, and consequently F5, are available only for neutrons and photons. This is done by tracing the pseudo-particle, without altering the original random walk path, from the collision site to the detector. The same process is also performed for source particles to provide the uncollided component. MCNP provides estimates of the quantities of interest for source particles alone (called direct contribution), due to uncollided particles, as well as due to the source and interactions combined (total contribution).

Line 86 corresponds to a point detector located along the y-axis and line 87-97 represents a ring detector. Line 96-107 represents tally type F4 for different position with respect to the offset angle α.

The remaining input data for MCNP are data cards composed of the following lines: particle designator (MODE), and problem cut-offs (NPS). Line number 62, defines a mode card which consist of the mnemonic mode followed by the type of particle to be transported (photons in this case), and line 83 defines the number of histories to be run by MCNP.

3.2.5 Variance Reduction Techniques

The variation reduction (biasing) techniques (VRT) for MCNP simulations can reduce the amount of computer time required for obtaining results of sufficient *precision* [3, 35, 37, 38, 39]. The main goal of all VRT is to decrease the relative error defined by Equation 2.25.

Generally, VRT are classified into three categories: modified sampling methods (e.g., source biasing, implicit capture, discrete angle biasing, forced collisions, and exponential transformation), population control methods (e.g., geometric splitting/Russian roulette, weight cutoff, weight-windows, and stratification), and semi-analytic methods (e.g., point detectors and DXTRAN). Among the VRT, the most effective and widely used technique in radiation transport problems for reducing the variance and computational time of a Monte Carlo simulations is the geometry splitting /Russian roulette method [38, 39].

The main objective of the splitting/Russian Roulette technique is to spend time sampling important regions (spatial cells) and less time sampling unimportant regions. It is easily done by subdividing the geometry of the problem into cells and assigning each cell i an importance I_i. As the particle of weight w_i passes from a cell with an importance I_i to a cell with higher importance $I_j(I_i < I_j)$, the particle is split into $v = I_j/I_i$ identical particles of weight w_i/v (see fig. 3.3). Conversely, if a particle of weight w_0 passes from a cell of importance I_i to a cell with lower importance $I_k(I_i < I_k)$, Russian roulette is played and the particle is killed with probability $1 - (I_i < I_k)$, or followed further with I_k/I_i and weight $w_i \times I_i/I_k$ [38, 39].

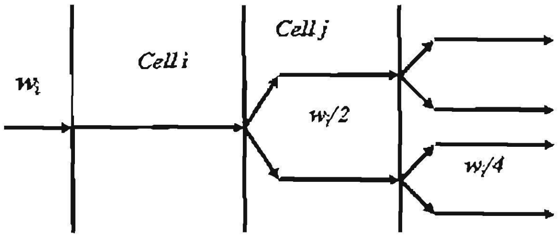

Figure 3.3: Schematic diagram illustrating the geometrical splitting technique.

In general, splitting decreases the history variance (decreases C); however, it increases the time per history (decreases N for a fixed amount of computer time); whereas Russian roulette decreases the time per history (increases N for a fixed amount of computer time).

The above VRT technique was applied in this work: line 3 in the input file (appendix A.1) represents the first cell numbered 1 for the VRT; other cells where the VRT was applied are shown in cells 16-21 (lines 22-27). Note that the importances are different for each cell representing the concept explained above.

3.3 Dose Rate Points Calculation

The dose rate points were calculated by using the following equations (based on Fig. 1.1 and Table 1.1):

$$Z = (Q + Y)\tan\alpha, \tag{3.2}$$

$$\Delta Z = \frac{(Q + Y)}{(\cos\alpha)^2}\Delta\alpha, \tag{3.3}$$

where Q is the distance between the source and slab, Y is the thickness of the slab. $\Delta\alpha$ was assumed to be plus or minus two degrees of each angle to represent the error within the calculation. This error is given by ΔZ.

Numerous calculations were performed for each material using the parameters and variables provided in Table 1.1, but only one example will be demonstrated here using the input file of MCNP provided in appendix A.1 (concrete with 35 cm thickness). The major and the minor radii of the tori from lines 42-53 (6^{th} and 8^{th} column) represent the dose rate points for different offset angles and ΔZ calculated using Eqs. (3.2, 3.3).

4 MicroShield Results

The MicroShield geometrical model and procedures described in chapter 3 were used to determine a set of effective dose rates (both uncollided and collided) for the materials listed in Table 4.1 at seven photon energies (0.3, 0.5, 0.75, 1, 1.5, 2, and 3 MeV). In addition, from the uncollided and collided effective dose rates the exposure build-up factors were calculated.

For each photon energy, calculations were performed at 12 offset angles (0, 10, 15, 20, 25, 30, 35, 40, 45, 50, 55, and 60 degrees) for various materials thickness as listed in Table 4.1. The position of the source from the shield was 10% of the maximum thickness of each material (i.e., 2 *cm* for lead, 5 *cm* for iron, and 25 *cm* for concrete). The effective dose rate points were calculated using equation 3.2 described in section 3.3 in chapter 3. The results for representative MS cases are presented in the following sections.

Table 4.1: Materials, physical properties, and slab thickness used for dose rate calculations with MS.

Material	density (g/cm^3)	slab thickness (cm)
Lead	11.37	1, 3, 7.5, 10, 15, 20
Iron	7.86	2, 7, 18, 25, 37.5, 50
Concrete	2.35	10, 35, 90, 125, 187.5, 250

4.1 Effective Dose Rates

The presentation of results begins with focus on the different lead thicknesses, as lead is a primary photon shielding material. Shown in Figure 4.1 are the effective dose rates for photon energies ranging from 0.3-3 MeV as a function of the offset angle α. Of particular interest is the noticeable downward trend in the effective dose rates with respect to increasing offset angle for all photon energies and lead thicknesses. Furthermore, for each material thickness, the effective dose rate decreases with decreasing photon energy. The behavior of lead also applies for iron and concrete (see Figures 4.2 and 4.3).

The dose rate at low photon energy for 0.3-0.5 MeV, and larger lead thicknesses (see Figures 4.1: (d), (e) and (f)) present change in the continuous and smooth expected behavior. Such problem is also observed for iron (see Figure 4.2: (f)) and concrete (see Figures 4.3: (e) and (f)). This numerical saturation, present in every case at 10^{-24} mSv/hr, could be due to the very low dose rate values with respect to the intensity of the source used in these calculations. The dependence of this saturation value on the intensity of the source might be related to the numerical accuracy of the MS software and it could be further investigated, but for this particular study the numerical saturation only affects results in the non-relevant dose rate region.

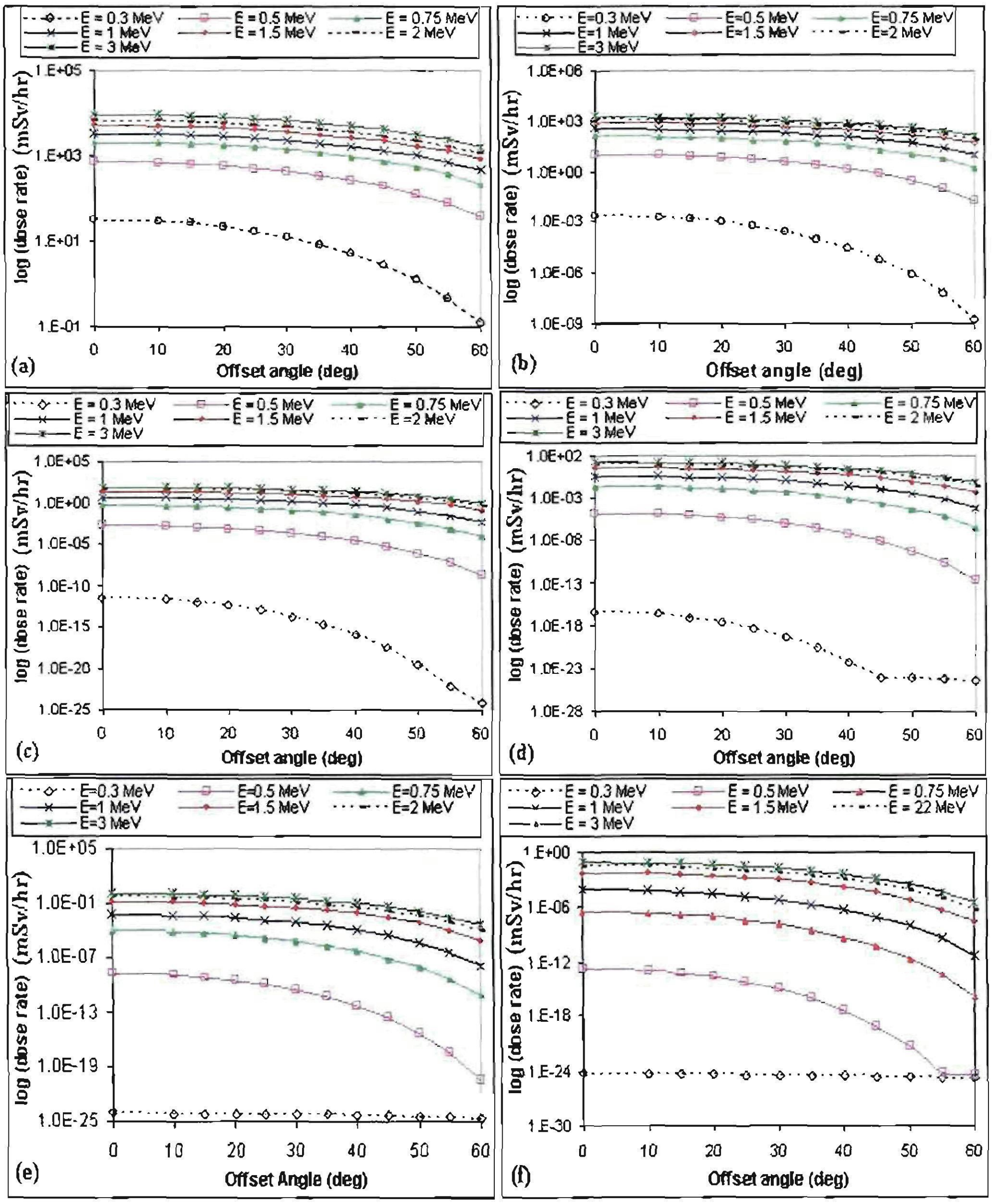

Figure 4.1: Effective dose rates as a function of the offset angle for lead thicknesses of (a) 1 *cm*, (b) 3 *cm*, (c) 7.5 *cm*, (d) 10 *cm*, (e) 15 *cm*, and (f) 20 *cm*.

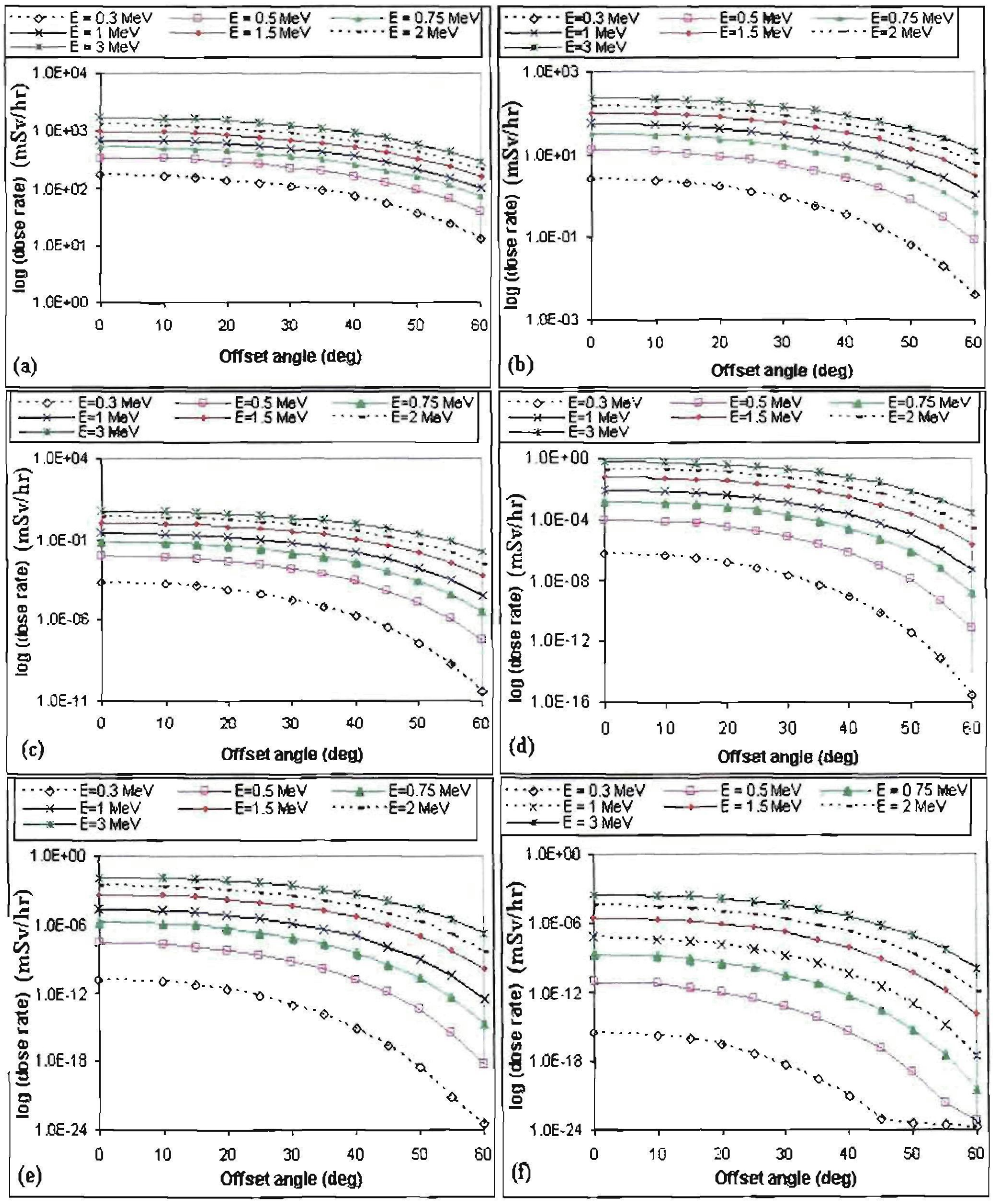

Figure 4.2: Effective dose rate as a function of the offset angle for iron thicknesses of (a) 2 *cm*, (b) 7 *cm*, (c) 18 cm *cm*, (d) 25 *cm*, (e) 37.5 *cm*, and (f) 50 *cm*.

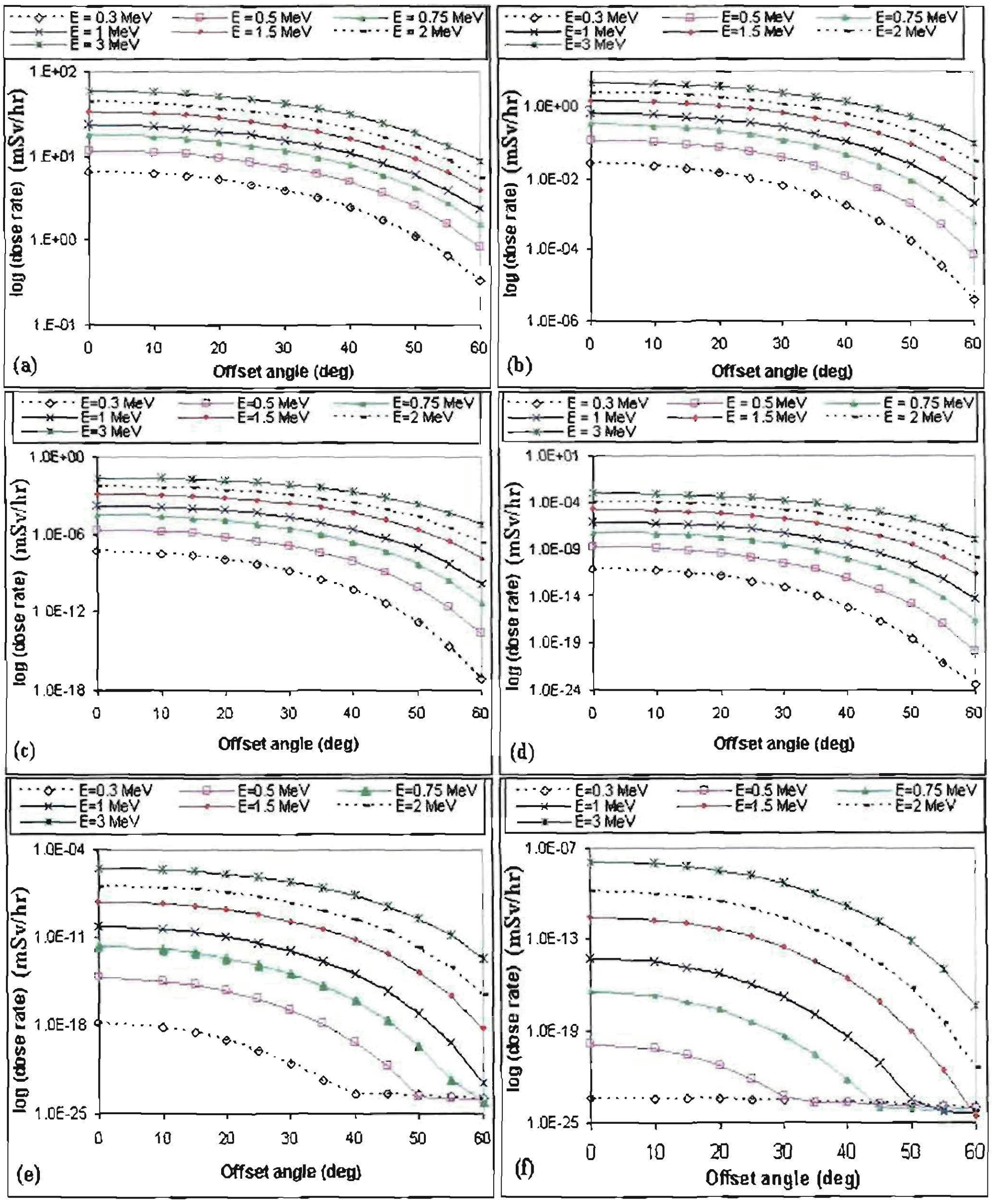

Figure 4.3: Effective dose rate as a function of the offset angle for concrete thicknesses of (a) 10 *cm*, (b) 35 *cm*, (c) 90 *cm*, (d) 125 *cm*, (e) 187.5 *cm*, and (f) 250 *cm*.

4.2 Exposure Build-Up Factors

Figures 4.4, 4.5, and 4.6 display build-up factors with respect to the offset angle for photon energies ranging from 0.3-3 MeV and various thicknesses of lead, iron, and concrete shielding. As shown in these figures, there is a significant increase of build-up factors with respect to increasing offset angle relative to normal, for photon energies ranging from 0.5-3 MeV and various materials thickness. At low energies (i.e. 0.3 MeV) the build-up factor increases much slower with increasing offset angle. As the thickness increases the increase in build-up factors decreases. At deep penetration the variations of build-up factors with respect to α increase very quickly. From Figure 4.7 it can be observed that at low photon energies (0.3-0.5 MeV), the build-up factors are extremely high for lead (in the order of 10^{48}), and increase with increasing material thickness. A Similar trend is further noted for iron and concrete at photon energies ranging from 0.3-0.5 MeV. For iron and concrete the build-up factors are in the order of 10^{12}, and 10^{32}, respectively.

Another interesting observation is the discontinuous behaviour of the exposure build-up factors as shown in Figure 4.6 (f) for 1.5 MeV and Figure 4.7 (a), (b), (c), and (d) at the various energy levels. This numerical problem is only present at the points where the numerical values of the effective dose rate saturates (see previous section).

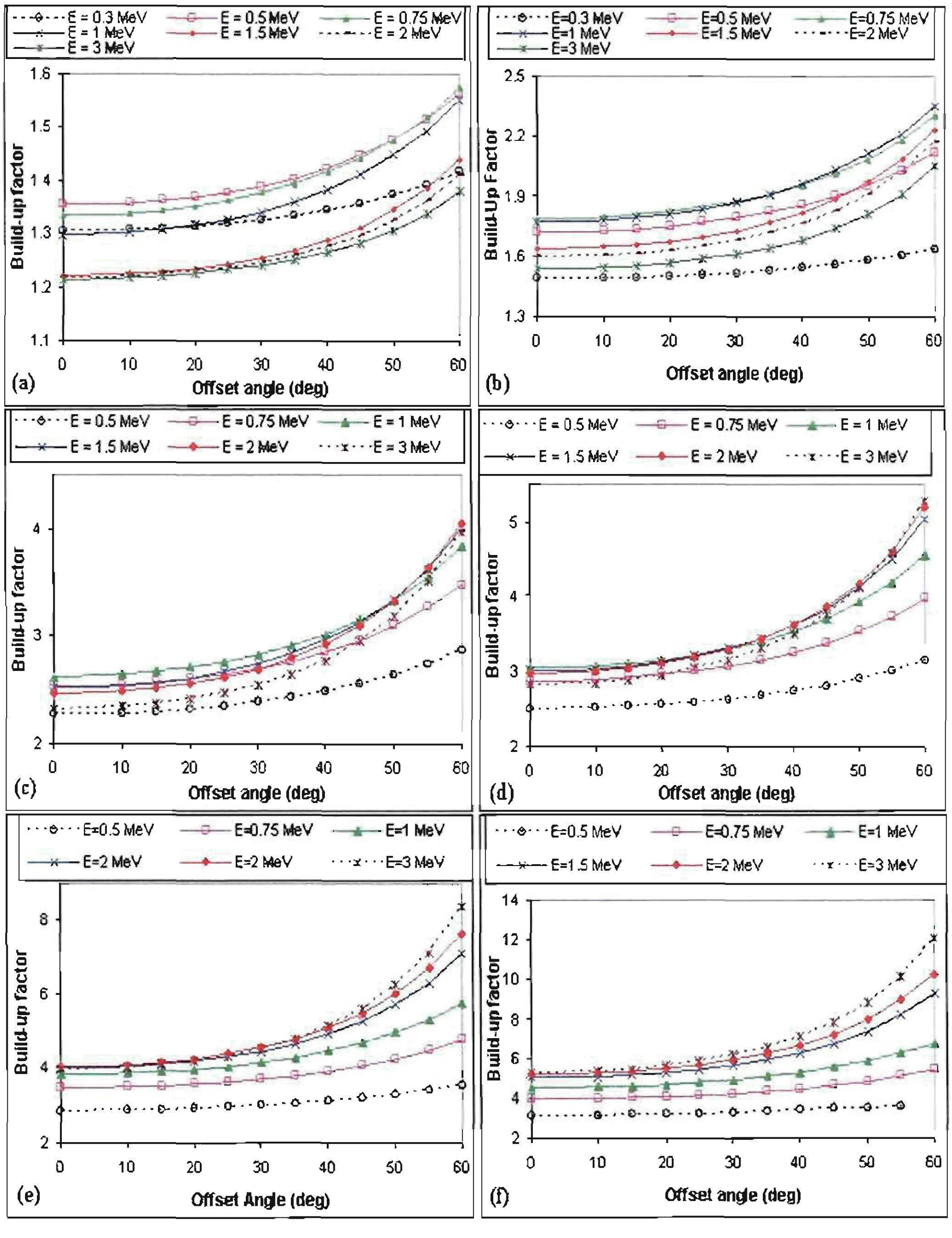

Figure 4.4: Build-up factors as a function of the offset angle for lead thicknesses of (a) 1 *cm*, (b) 3 *cm*, (c) 7.5 *cm*, (d) 10 *cm*, (e) 15 *cm*, and (f) 20 *cm*.

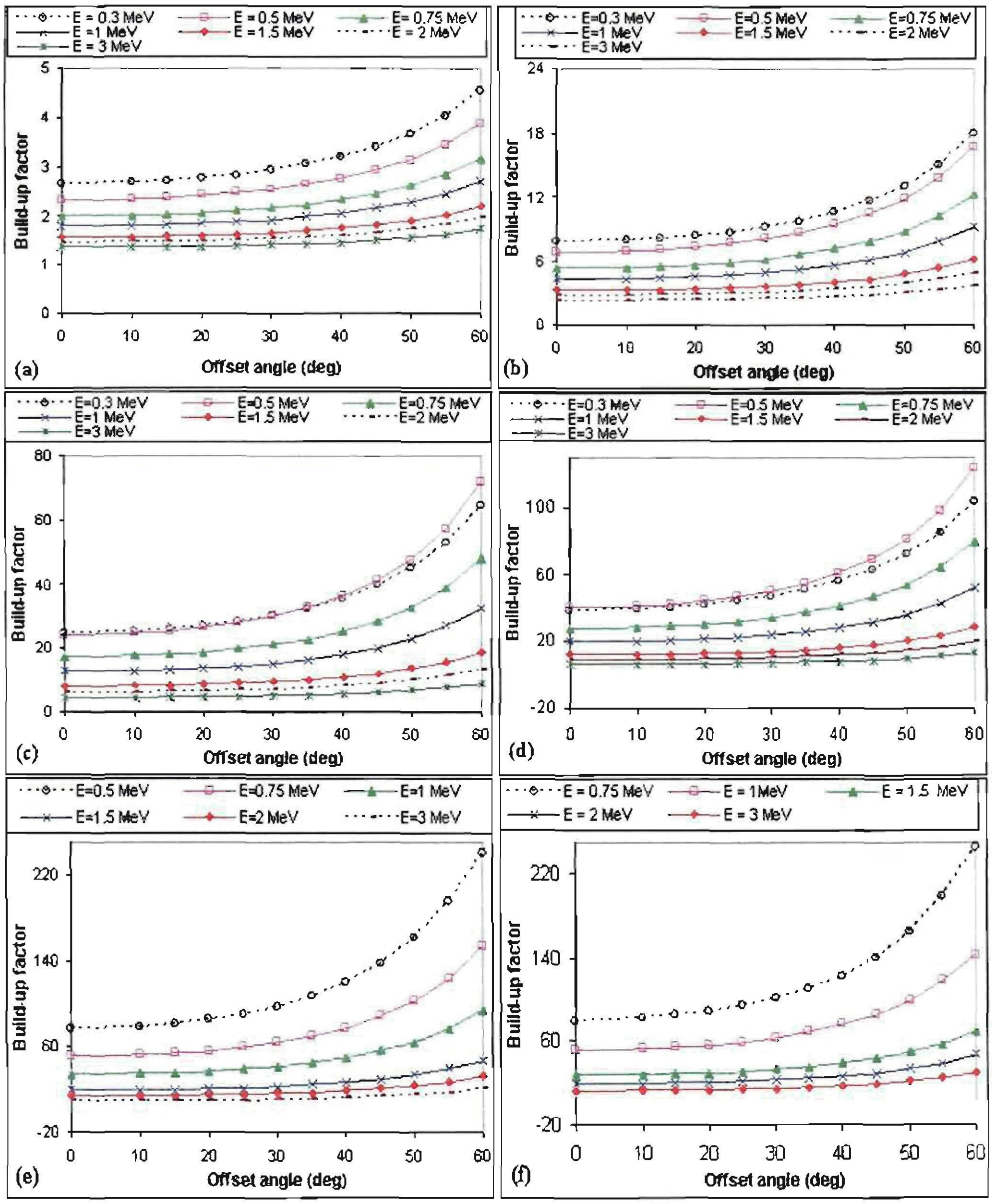

Figure 4.5: Build-up factors as a function of the offset angle for iron thicknesses of (a) 2 *cm*, (b) 7 *cm*, (c) 18 cm *cm*, (d) 25 *cm*, (e) 37.5 *cm*, and (f) 50 *cm*.

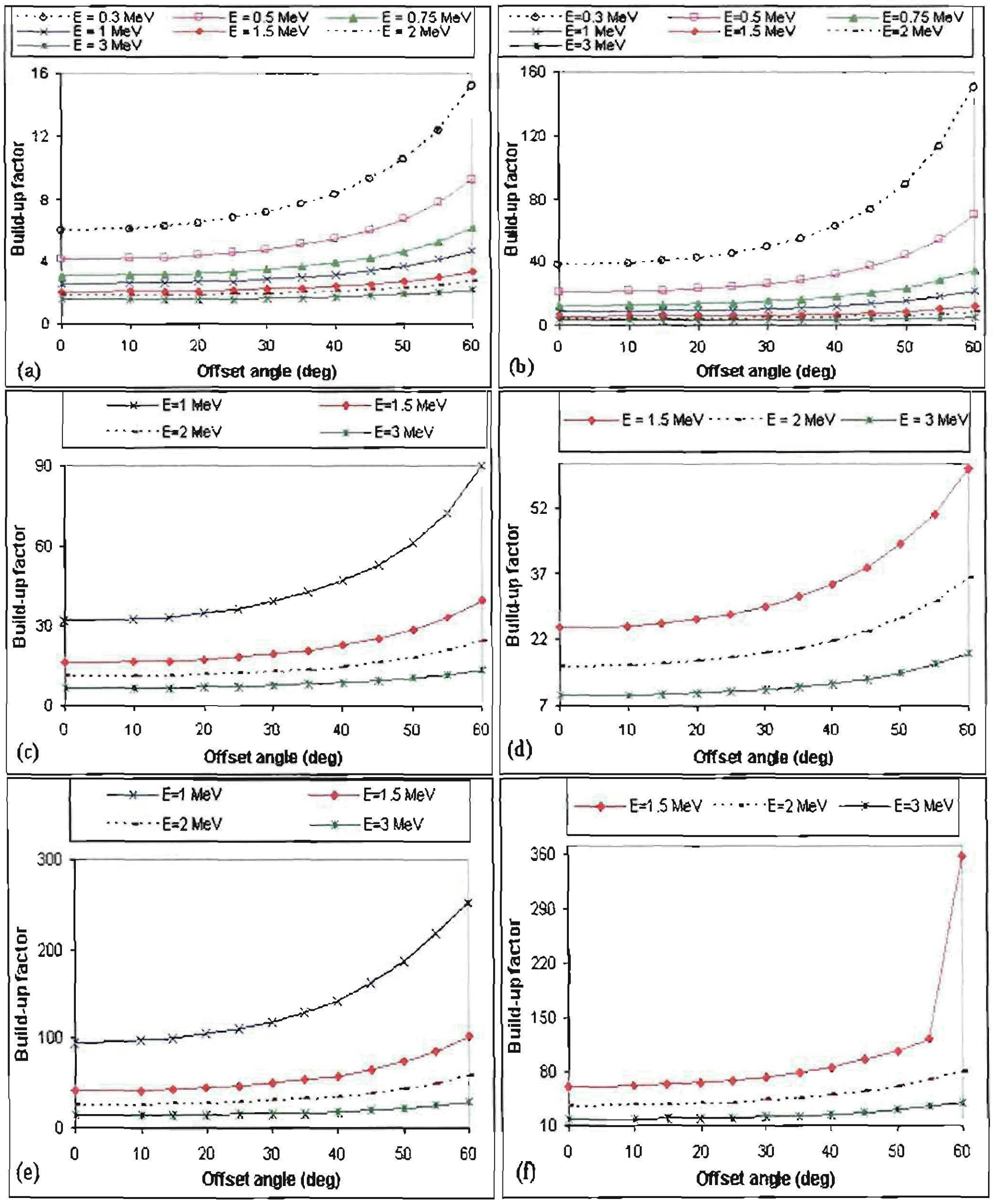

Figure 4.6: Build-up factors as a function of the offset angle for concrete thicknesses of (a) 10 *cm*, (b) 35 *cm*, (c) 90 *cm*, (d) 125 *cm*, (e) 187.5 *cm*, and (f) 250 *cm*

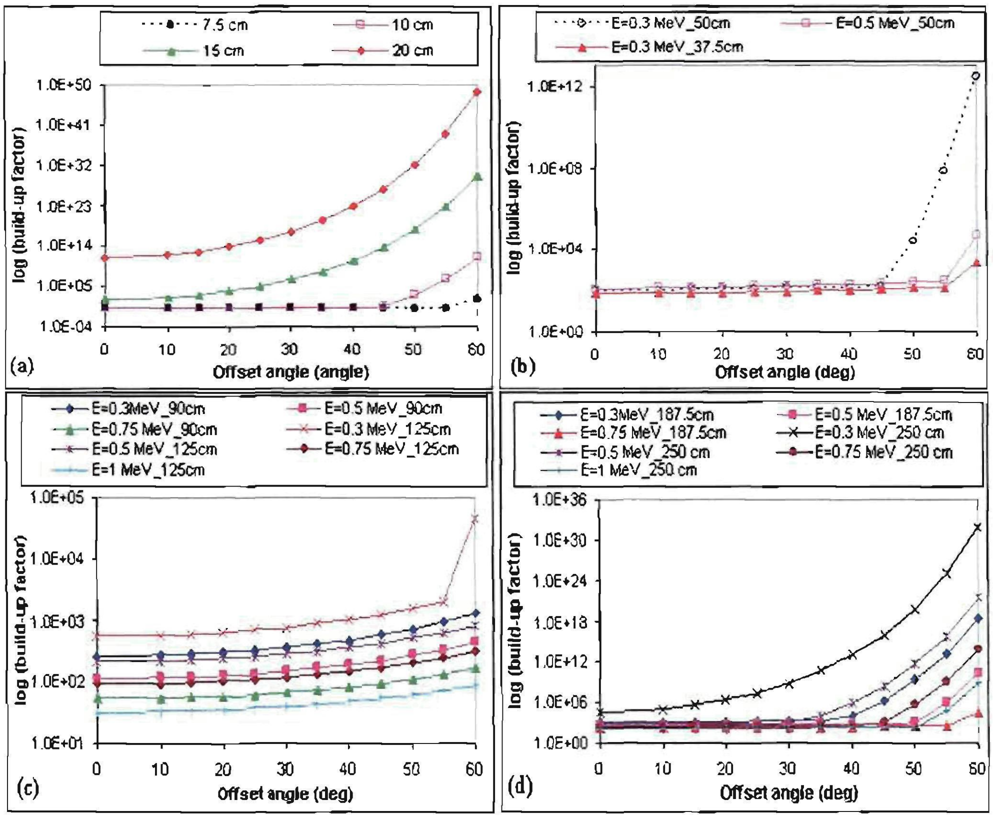

Figure 4.7: Increasing of build-up factors as a function of the offset angle for (a) lead with 7, 10, 15, and 20 *cm* for photons of 0.3 MeV, (b) iron with 37.5 and 50 *cm* for photons of 0.3-0.5 MeV, and (c-d) concrete with 90, 125, 187.5, and 250 *cm* for photons of 0.3-0.5 MeV.

4.3 Qualitative and Quantitative Analysis of Results

As indicated in figures 4.1-4.3, the dose rates simulated by MS show a decreasing trend with increasing offset angle with respect to the photon energies and various materials thickness. To determine why these trends are observed, a qualitative and quantitative analysis of slab thickness is presented.

In Figure 4.8, photon traversing in path length r_0 with offset angle $\alpha_0 = 0$ degrees may experience an interaction (or traverse without an interaction) within the shield subject to scattering into an angle detected by $Klein - Nishina$ formula [18]. Since the photon is normally incident on the slab, the azimuthal component of scattering angle has no influence as to the remaining path length that a photon must traverse to exit the slab. This implies that all scattered photons exit the slab with equal probability. In the case of a photon traversing in path lengths r_1 and r_2 with offset angles α_1 and α_2, the azimuthal component of the $Klein - Nishina$ scattering angle has a significant effect on whether the scattered photon will exit the slab. For example, should a photon scatter at an angle such that it follows the "short" escape path of length optical thickness, x_{short}, the probability for it to exit without further scattering is $e^{-x_{short}}$. The same is true when that photon scatters into the angle that takes it along the "long" escape path. Hence quantitatively, $e^{-x_{short}} > e^{-x_{long}}$ that is, particles scattered along the short path length are more likely to escape the slab.

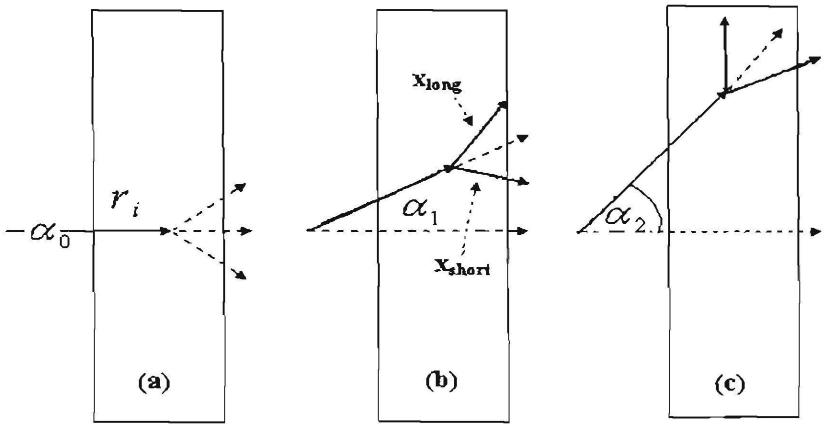

Figure 4.8: Escape path differences for (a) normal, (b) moderate, and (c) extreme offset angles.

Qualitatively, one can see that the extent by which the short and long escape paths differ depends heavily on depth in the shield at which the collision occurs, and the scattering angle itself. Particles escaping along the short path cross the exit surface with angles less severe (relative to normal) than those escaping along the long path and thus contribute less to the flux across the slab's exit surface. As the offset angle increases, both the normal thickness and short optical escape path length x_{short} decrease significantly. This allows these particles to have a shorter optical path length that is more in the normal incident direction. It enables these photons to have a higher probability of escaping the slab with fewer interactions. As a result, the contribution to the total exit flux decreases with increasing photon offset angle and leads to an increase in the build-up factor value.

Equation 2.12 which represents an isotropic point source, can easily be used to clarify the decreasing trend of the dose rate and increasing of build-up factor with respect to the offset angle. Equation 2.12 indicates that as the distance between the source and the detector point r_i increases, the total flux ϕ_T decreases with the square of this distance. For example, in Figure 4.8 $\phi_0 > \phi_1 > \phi_2$ because $r_2 > r_1 > r_0$ for α_0, α_1, and α_2. Furthermore, the exponential function in equation 2.12 is one of the factors contributing toward a decreasing trend of the total flux. The distance x_i traveled by photons in the shielding material differs with respect to the cosine of the offset angle α_i (or with respect to the normal). The effect of the cosine due to the offset angle results in x_i increasing, and in turn a decrease of the exponential function (i.e., $e^{-\mu x_0} > e^{-\mu x_1} > e^{-\mu x_2}$), and finally a decreasing trend of the dose rate.

From equation 2.12 the build-up factor B is defined as ϕ_T/ϕ_u $(1 + \phi_s/\phi_u)$. It is clear that the value of the build-up factor is always greater than one due to the extra photon scattering component. The scattering component of photons increases with increasing x_i with respect to the cosine of the offset angle α_i. In other words, the photon scattering component depends on x_i and the distance r_i travelled by photons. Photons traveling longer distances r_i have a higher probability of interacting with the material more than once. This effect causes the ratio ϕ_s/ϕ_u to increase, and therefore, resulting in increasing build-up factors.

5 Comparison between MicroShield and MCNP Results

In this chapter, the redefinition of maximum shielding thickness, comparison of MS with MCNP results, and the definition of limit of applicability of MS are presented.

5.1 Redefinition of Maximum Shielding Thickness

As explained in chapter 4, the MS simulations have shown that for all various larger materials thickness and at low photon energies (0.3-0.5 MeV) the effective dose rates as a function of the offset angle saturates in the order of $10^{-24} - 10^{-25}$ mSv/hr. In addition, the effective dose rates at various larger materials thickness are observed to be very low in comparison with the natural background radiation (2 mSv/y). As a result of these effects, the maximum shielding thickness for all the materials to be used in the comparison between MS and MCNP calculations were redefined as shown in Table 5.1.

Table 5.1: Redefined maximum shielding thickness for various materials.

Material	density (g/cm^3)	slab thickness (cm)
Lead	11.37	1, 3, 7.5, 10
Iron	7.86	2, 7, 18, 25
Concrete	2.35	10, 35, 90, 125

5.2 Comparison of Results

For each of the materials and three photon energies (0.3, 0.75, and 3 MeV), MS and MCNP effective dose rates were calculated at various materials thickness as listed in Table 5.1, and at the 12 offset angles. As Monte Carlo calculations are computationally more expensive, the goal was not to repeat each MS calculation, but to perform sufficiently simulations so that a convincing argument can be made regarding the limit of applicability of MS code compared to a different method. MicroShield and MCNP effective dose rate results are tabulated in Appendix A.2-4.

In general, the two codes demonstrate reasonable similarities as shown in Figures 5.1 and 5.2 for photon energies of 0.3, 0.75, and 3 MeV at different slab thicknesses of lead, iron, and concrete. From these Figures, it can be observed that for the selected materials and photon energies, the effective dose rate values of both codes decreased as a function of increasing offset angle. Another trend that occurred for the investigated materials and incident photon energies studied was that the effective dose rates of the two codes began to differ substantially for photons at the highest offset angles. This means that the point-kernel calculations of MS underestimates the effective dose rates measured on the outer surface of the slabs for photons at the highest offset angles. In addition, these Figures indicates that the shielding effectiveness per unit mass increases as the composition of the shield changes from heavier to lighter mass materials. For example, at 3 MeV, lead is the most effective gamma shielding material (dose rates are in the order of 10^{-2} to 10^{1}-see Figure 5.1(a)) in comparison to concrete (dose rates are in the order of 10^{0} to 10^{1}-see Figure 5.2(a)) for shielding thickness of $10cm$. Similarly, lead is the most effective gamma shielding material (dose rates are in the order of 10^{0} to 10^{1}-see Figure 5.1(a)) in comparison to iron (dose rates are in the order of 10^{1} to 10^{2}-see Figure 5.1(d) for shielding thickness of approximately $7cm$. The reasons for these trends are the same as explained in section 4.3.

The major difference between MS and Monte Carlo (MCNP) methods lies in the treatment of the energy variable, evaluation of build-up factors, and theoretical model. Photons in Monte Carlo exist at specific energies (i.e., continuous) detected by the laws of interaction physics, while the MicroShield incorporates the unabridged energy groups. The geometry defined in the dialog box does not correspond to the geometry used in the determination of the build-up factor, which was a broad beam with the outer surface of the slab as the detector. MicroShield uses the point-kernel method to break a line, area, or volume source into segments to compute the attenuation along the trajectory from the source element through any shield, and integrates the contributions at the receptor location from the large number of "point" sources. On the other hand, Monte Carlo solves the detailed physics of the photon transport in the real geometry. However, the statistical uncertainty in the MCNP calculations play a major role on the outcome of the error associated with the model investigated. In this work the absolute error obtained was very small in such a way that error bars lie within the points. The small uncertainty in the results was achieved by running the cases for longer periods, or using variance reduction techniques based on splitting particles or Russian roulette. The relative errors of the MCNP calculations are, in general, lower than 1%. Only the cases where the transport of particles was numerically challenging (larger thickness, lower energy and large offset angles) had relative errors between 1% and 10%. Every MCNP result in this thesis has passed all the statistical tests performed on the tallies.

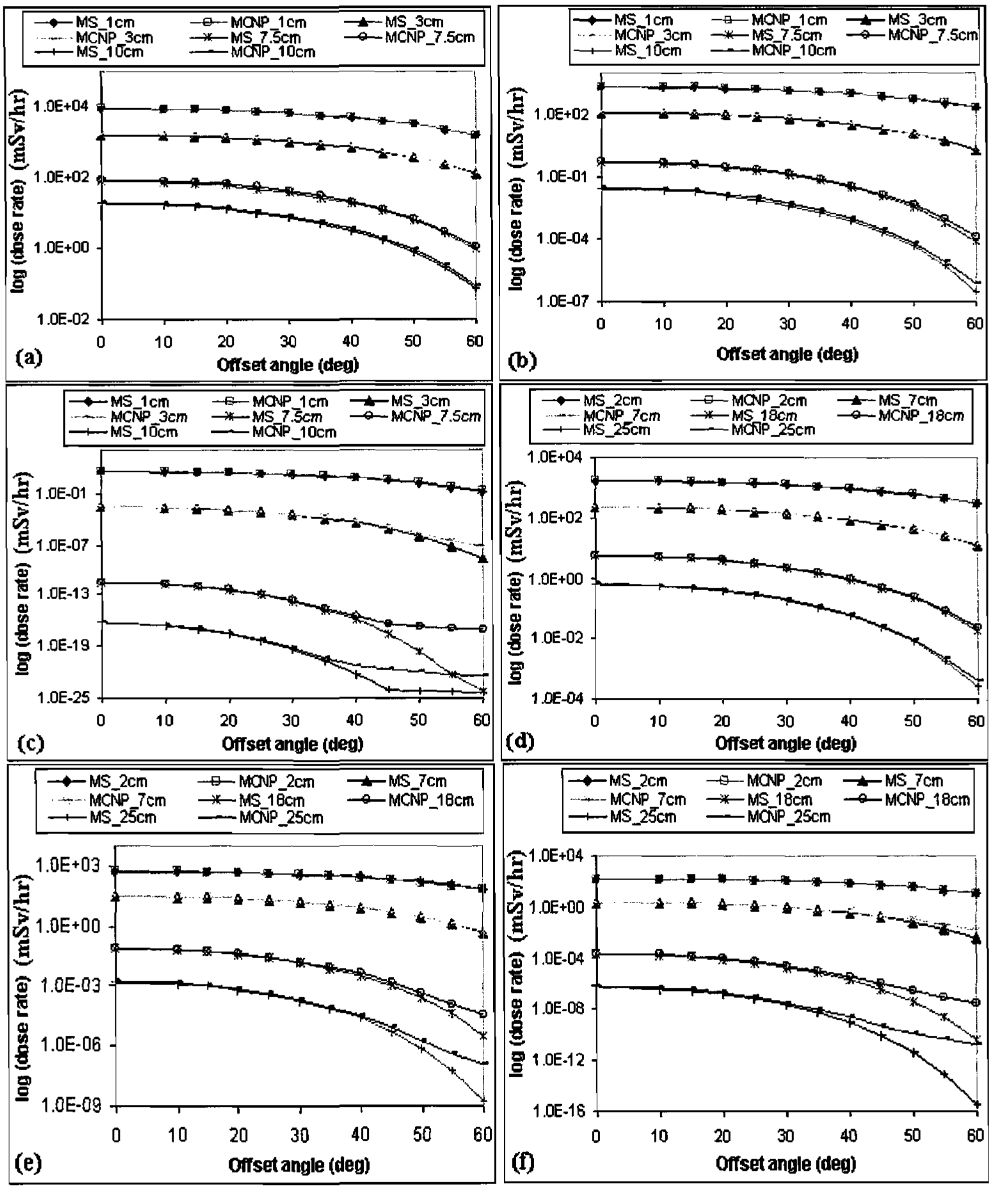

Figure 5.1: Effective dose rate as a function of the offset angle for various materials thickness of (a) lead: $E_\gamma = 3$ MeV, (b) lead: $E_\gamma = 0.75$ MeV, (c) lead: $E_\gamma = 0.3$ MeV, (d) iron: $E_\gamma = 3$ MeV, (e) iron: $E_\gamma = 0.75$ MeV and (f) iron: $E_\gamma =.3$ MeV.

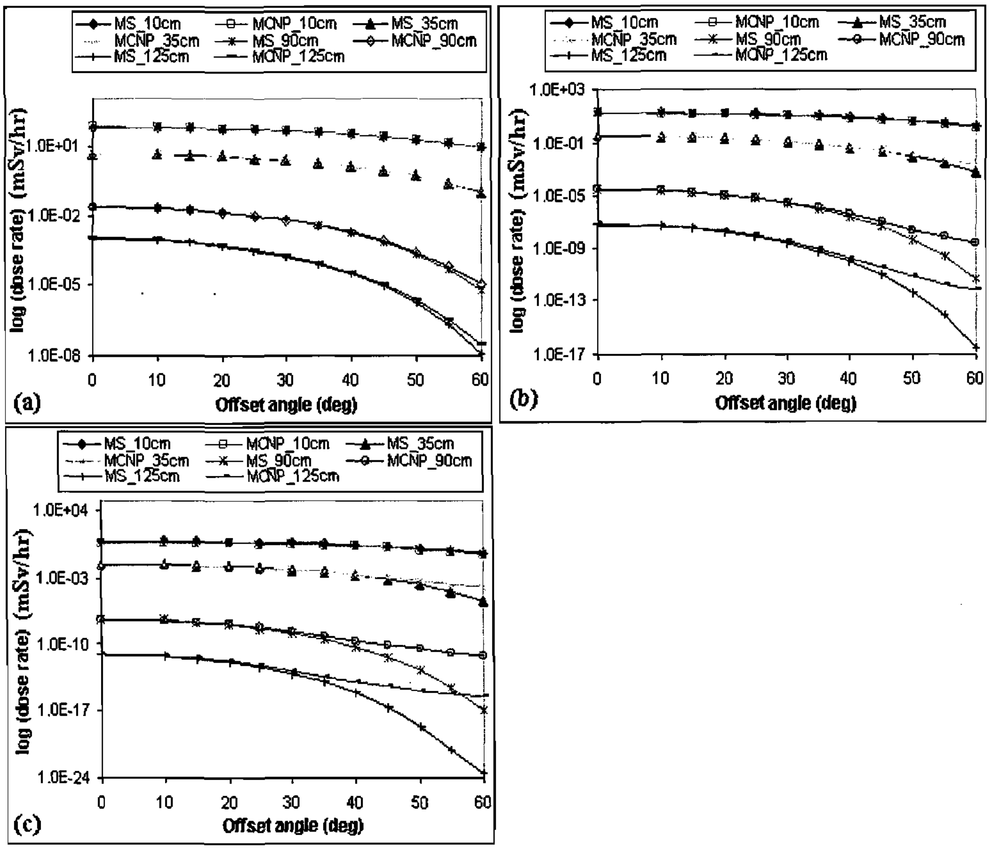

Figure 5.2: Effective dose rate as a function of the offset angle for various thicknesses of (a) concrete: $E_\gamma = 3$ MeV, (b) concrete: $E_\gamma = 0.75$ MeV and (c) concrete: $E_\gamma = 0.3$ MeV.

As shown in Figures 5.1, and 5.2, the results obtained with both MS and MCNP are in very good agreement for low offset angles. However, as the photon energy decreases and materials thickness increases some significant discrepancies arise with increasing offset angle.

To quantify the relative differences between MS and MCNP, the relative deviation (RD) was calculated using the following expression:

$$RD = \frac{(MS - MCNP)}{MCNP} \times 100\% \tag{5.1}$$

Figures 5.3, and 5.4 show the RD between MS and MCNP for photon energies of 0.3, 0.75, and 3 MeV at various materials thickness of lead, iron, and concrete. From Figure 5.3 (a) the RD between MS and MCNP results is constant at 1 and 3 *cm* of lead (i.e., within 0-9%) for photon energy of 3 MeV. However, at 7.5 and 10 *cm* the RD remain constant between 12-13% up to 40 degrees and then increases rapidly to 22% as a result of the increasing build-up factors with increasing materials thickness. Similar trends are observed in Figure 5.3 (b) for lead with RD increasing up to 60%; (d) and (e) for iron with RD increasing up to 98%; and Figure 5.4 (a) for concrete with RD increasing up to 58%.

For photon energies of 0.3-0.75 MeV, the RD between MS and MCNP results ranges from 0 to 30% at 1 *cm* of lead (see Figure 5.3 (c)); 0-13% at 2 *cm* of iron (see Figure 5.3 (f)); 0-25% at 10 *cm* of concrete (see Figure 5.4 (b) and (c)). From the same Figures and same photon energies, the remaining materials thickness of lead, iron, and concrete show an increasing trend of RD at very low offset angles ranging from 25-40 degrees and then saturates from 40-60 degrees.

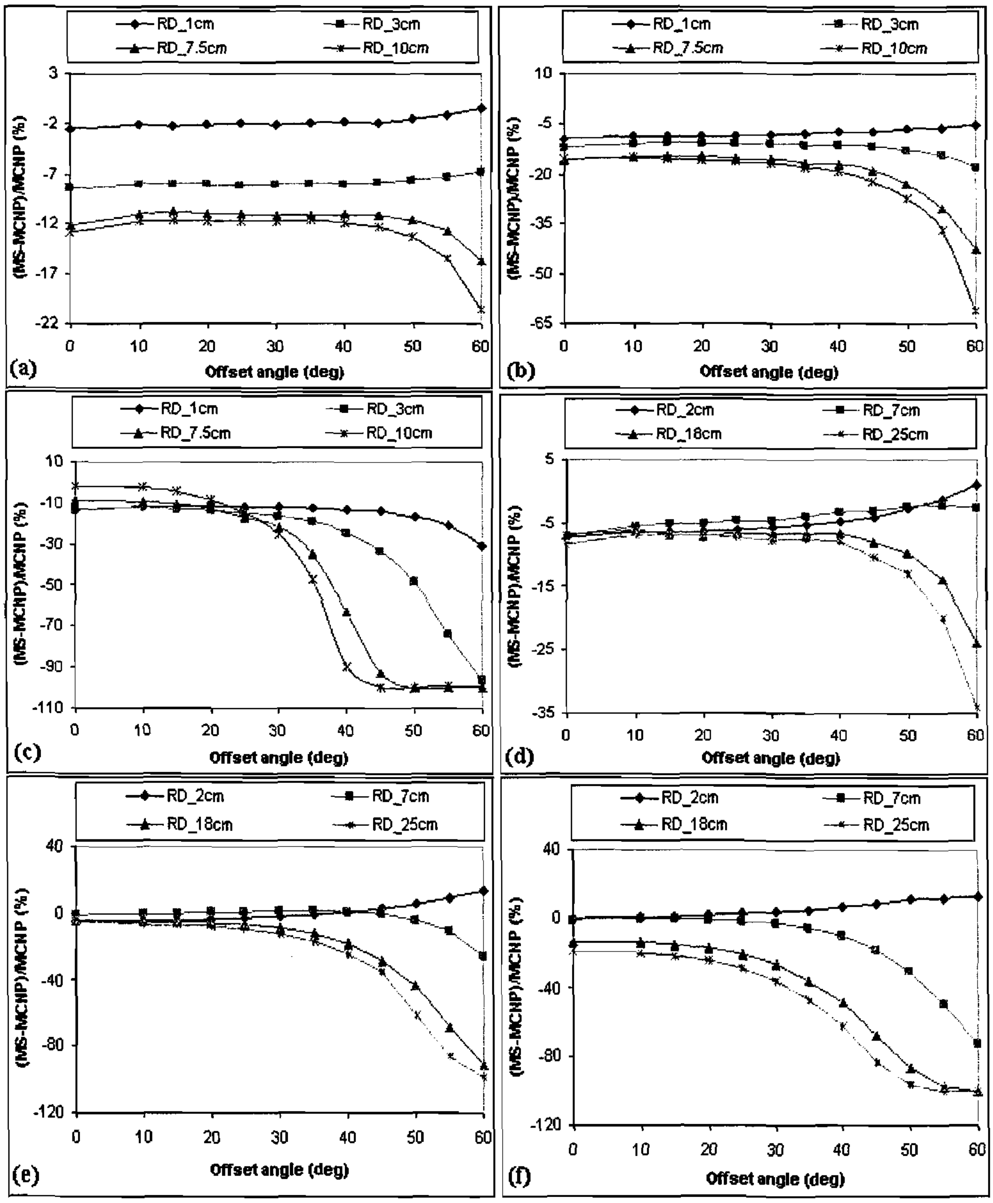

Figure 5.3: RD between MS and MCNP as a function of the offset angle for various materials thickness of (a) lead: $E_\gamma = 3$ MeV, (b) lead: $E_\gamma = 0.75$ MeV, (c) lead: $E_\gamma = 0.3$ MeV, (d) iron: $E_\gamma = 3$ MeV, (e) iron: $E_\gamma = 0.75$ MeV and (f) iron: $E_\gamma = 0.3$ MeV.

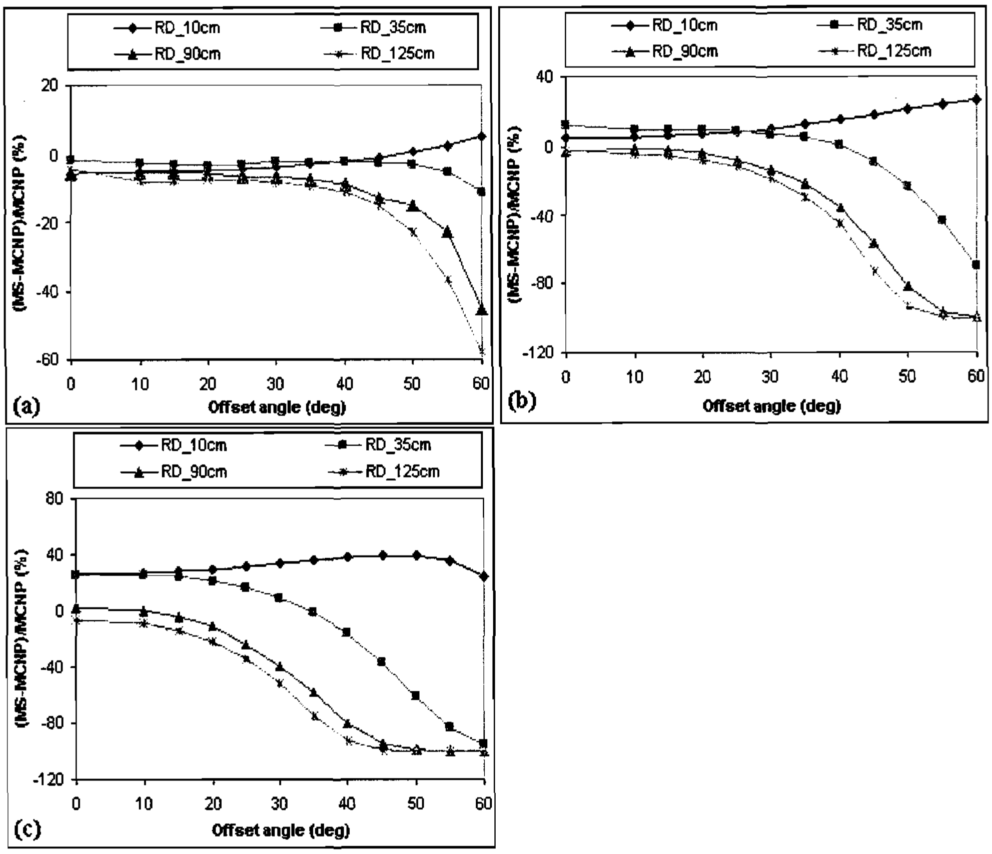

Figure 5.4: RD between MS and MCNP as a function of the offset angle for various thicknesses of concrete (a) $E_\gamma = 3$ MeV, (b) $E_\gamma = 0.75$ MeV and (c) $E_\gamma = 0.3$ MeV.

5.3 Definition of Limit of Applicability

The comparison between MS and MCNP calculations from the previous section have shown that as the photon energies decreased from high to low as well as the materials thickness increases, the effective dose rate values began to differ substantially for photons at highest offset angles. In addition, the RD of MS from MCNP simulations occurred at different offset angle and photon energies for lead, iron, and concrete. Therefore, to define the limit of applicability of MS in terms of the offset angle (defined as α_{max}), Figures 5.3 through 5.4 were used together with the maximum error of 30 % recommended by the MS manual [1].

The results defining the limits of applicability of MS in terms of the offset angle α are presented in Table 5.2 for photon energies of 0.3, 0.75, and 3 MeV at materials thickness of lead, iron, and concrete. The results presented in this work are mainly applicable for mono-energetic γ-rays only. Complete results are tabulated in Appendix A.5-6.

Table 5.2: Limits of applicability of MicroShield for various materials thickness of lead, iron, and concrete.

Lead thickness (*cm*)	α_{max} at 3 MeV	α_{max} at 0.75 MeV	α_{max} at 0.3 MeV
1	60	60	55
3	60	60	40
7.5	60	55	30
10	60	50	30
Iron thickness (*cm*)	α_{max} at 3 MeV	α_{max} at 0.75 MeV	α_{max} at 0.3 MeV
2	60	60	60
7	60	60	45
18	60	45	30
25	55	40	25
Concrete thickness (*cm*)	α_{max} at 3 MeV	α_{max} at 0.75 MeV	α_{max} at 0.3 MeV
10	60	60	60
35	60	50	40
90	60	45	30
125	55	35	25

6 Conclusion

The ease of use and low computer time in finding solutions are advantages that make MS a useful scoping analysis tool for the evaluation of gamma radiation shielding. An important drawback is related to the behavior of MS build-up factors for different γ-ray energies and geometries as well as their limit of applicability due to the offset angle from the symmetry axis.

The aim of this research was to evaluate MS build-up factors and define their limits of applicability with respect to the photon offset angle α. In order to evaluate the behavior of MS build-up factors and define their limits of applicability, the effective dose rates obtained from MS and MCNP codes were compared. The investigation in this work was performed using an isotropic point source with various material thicknesses of lead, iron, and concrete for photon energies ranging from 0.3 to 3 MeV.

Despite the differences of MS and MCNP geometries, photon energies treatment, cross-sections data, and the theoretical models used to calculate the effective dose rates, there is generally good agreement with the build-up factors for offset angles ranging from approximately 0 to 30 degrees. However, the results of both codes are different at the highest offset angles. To quantify the difference between MS and MCNP the relative deviation between the two codes was evaluated. From the relative deviation results, the limit of applicability of MS with respect to the recommended maximum error of 30% from the MS manual was defined.

In summary, for a certain range of offset angles around the symmetry axis, the comparison of effective dose rates obtained with MCNP show that reliable radiation shielding calculations can be obtained with MS. Based on the criteria defined in section 5.3, offset angles smaller than 25 degrees always compare well with MCNP, regardless of γ-ray energy, material type and thickness. However, for offset angles greater than 25 degrees some cases (very thick shielding, very low energy and high Z material) could be affected by the use of build-up factors and the analyst should ensure that the case modeled is still within the limit of applicability.

The work done in this project has been concentrated on simple slab geometry. Future projects may involve the evaluation of MS build-up factors and their limit of applicability for complex geometries such as cylinder, line and volumetric shielding.

Appendices

The following appendices include a sample input file of one of the materials (concrete) implemented into the MCNP code. This section also incorporates the compilation of the comparison effective dose rates and Relative Deviation between MS and MCNP for all three shielding materials over the photon energies of 3, 0.75, and 0.3 MeV.

Appendix A.1 : Sample Input File for MCNP code

The MCNP input file contains information about the problem geometry, the source and the materials involved. An example of the input file that has been used in the present study is shown below (for concrete). The input file is divided into cards. The cell cards and the surface cards define the geometry of the problem. The data cards contain all other information that needs to be defined in an MCNP problem like the definition of the source and the materials. See the MCNP manual [3] for details.

```
****************************************************************************
Title: Dose Rate Calculation for Concrete
c Cell Cards
1  1 -2.35 -1 2 4 -5 6 -22          imp:p=1                $ Shielding (slab)
2  0 -7 (1: -2: 3: -4: 5: -6) 8 11 12 13 14 15 16 17 18 19 20 21 imp:p=1 $ Air
c
c *************** Tori for Tallies *****************************************
c
4  0 -8  imp:p=1.11E+01
5  0 -11 imp:p=1.11E+01
7  0 -13 imp:p=1.11E+01
9  0 -15 imp:p=1.11E+01
10 0 -16 imp:p=1.11E+01
11 0 -17 imp:p=1.11E+01
12 0 -18 imp:p=1.11E+01
13 0 -19 imp:p=1.11E+01
14 0 -20 imp:p=1.11E+01
15 0 -21 imp:p=1.11E+01
c
c *************** Variance Reduction *************************************
16 1 -2.35 -1 4 -5 6 22 -23 imp:p=1.51E+00
17 1 -2.35 -1 4 -5 6 23 -24 imp:p=2.17E+00
18 1 -2.35 -1 4 -5 6 24 -25 imp:p=3.23E+00
```

```
19 1 -2.35 -1 4 -5 6 25 -26 imp:p=4.87E+00
20 1 -2.35 -1 4 -5 6 26 -27 imp:p=7.34E+00
21 1 -2.35 -1 4 -5 6 27 -3  imp:p=1.11E+01
c
 c *************** Outside World *****************************************
c
22 0          7                 imp:p=0

c Surface Cards
1  PZ 3000
2  PY 0
3  PY 35
4  PZ -3000
5  PX 3000
6  PX -3000
7  SO 6020
8  SQ 0.227533 420 0.227533 0 0 0 -1 0 35.0501 0
11 TY 0 35.0501 0 10.58985404 0.05 2.1616
12 TY 0 35.0501 0 16.09256061 0.05 2.2470
13 TY 0 35.0501 0 21.85952698 0.05 2.3742
14 TY 0 35.0501 0 28.00595774 0.05 2.5524
15 TY 0 35.0501 0 34.67537743 0.05 2.7954
16 TY 0 35.0501 0 42.05462142 0.05 3.1246
17 TY 0 35.0501 0 50.39728058 0.05 3.5730
18 TY 0 35.0501 0 60.06233184 0.05 4.1937
19 TY 0 35.0501 0 71.58136987 0.05 5.0753
20 TY 0 35.0501 0 85.78315345 0.05 6.3745
21 TY 0 35.0501 0 104.0424468 0.05 8.3896
c *************** Variance Reduction**********************************
22 PY 5
23 PY 10
24 PY 15
25 PY 20
26 PY 25
27 PY 30

c Data Cards
MODE P
m1 13027.66c  -4.380E-02    $ Al-27
   20000.66c  -5.760E-02    $ Ca-nat
   26054.66c  -5.984E-04    $ Fe-54
```

```
     26056.66c -9.646E-03   $ Fe-56
     26057.66c -2.248E-04   $ Fe-57
     26058.66c -3.045E-05   $ Fe-58
     1001.66c  -3.000E-03   $ H-1
     19000.66c -2.250E-02   $ K-nat
     12000.66c -6.400E-03   $ Mg-nat
     11023.66c -1.000E-02   $ Na-23
     8016.66c  -4.834E-01   $ O-16
     15031.66c -1.000E-04   $ P-31
     16000.66c -2.200E-03   $ S-nat
     14000.60c -3.307E-01   $ Si-nat
     2004.66c  -2.979E-02   $ He-4
     27059.66c -2.000E-06   $Co-59
     73181.66c -5.000E-06   $ Ta-181
c ***************************************************************
SDEF ERG 3 WGT 3.7E10 POS 0 -25 0  $ isotropic source with E=3MeV
nps 3E6
 f005:p 0 35     0          0.03 $ point detector (alpha=0)
 f015Y:p 35 10.58985404 0.03 $ ring Detector (alpha=10)
 f025Y:p 35 16.09256061 0.03 $ ring Detector (alpha=15)
 f035Y:p 35 21.85952698 0.03 $ ring Detector (alpha=20)
 f045Y:p 35 28.00595774 0.03 $ ring Detector (alpha=25)
 f055Y:p 35 34.67537743 0.03 $ ring Detector (alpha=30)
 f065Y:p 35 42.05462142 0.03 $ ring Detector (alpha=35)
 f075Y:p 35 50.39728058 0.03 $ ring Detector (alpha=40)
 f085Y:p 35 60.06233184 0.03 $ ring Detector (alpha=45)
 f095Y:p 35 71.58136987 0.03 $ ring Detector (alpha=50)
 f105Y:p 35 85.78315345 0.03 $ ring Detector (alpha=55)
 f115Y:p 35 104.0424468 0.03 $ ring Detector (alpha=60)
 f004:p  4                   $ flux in a cell  (alpha=0)
 f014:p  5                   $ flux in a cell  (alpha=10)
f024:p  6                    $ flux in a cell  (alpha=15)
f034:p  7                    $ flux in a cell  (alpha=20)
f044:p  8                    $ flux in a cell  (alpha=25)
f054:p  9                    $ flux in a cell  (alpha=30)
f064:p 10                    $ flux in a cell  (alpha=35)
f074:p 11                    $ flux in a cell  (alpha=40)
f084:p 12                    $ flux in a cell  (alpha=45)
f094:p 13                    $ flux in a cell  (alpha=50)
f104:p 14                    $ flux in a cell  (alpha=55)
f114:p 15                    $ flux in a cell  (alpha=60)
```

```
c ******************************************************************
c Annals of the ICRP - ICRP 74 - Vol 26 - Nos 3/4, 1996, pp. 179-200
c Data taken from PBMR database 026103 Rev.2b
c ******************************************************************
#    DE0         DF0
     1.00E-02    2.20E-07
     1.50E-02    2.99E-06
     2.00E-02    3.78E-06
     3.00E-02    2.92E-06
     4.00E-02    2.30E-06
     5.00E-02    1.98E-06
     6.00E-02    1.84E-06
     8.00E-02    1.91E-06
     1.00E-01    2.20E-06
     1.50E-01    3.20E-06
     2.00E-01    4.32E-06
     3.00E-01    6.48E-06
     4.00E-01    8.57E-06
     5.00E-01    1.05E-05
     6.00E-01    1.24E-05
     8.00E-01    1.58E-05
     1.00E+00    1.87E-05
     1.50E+00    2.48E-05
     2.00E+00    3.10E-05
     3.00E+00    4.00E-05
     4.00E+00    4.82E-05
     5.00E+00    5.58E-05
     6.00E+00    6.34E-05
     8.00E+00    7.78E-05
     1.00E+01    9.22E-05
*************************************************************************
```

Appendix A.2:

Comparison of effective dose rates (mSv/hr) between MS and MCNP for lead.

α (deg.)	MS_1cm	MCNP_1cm	MS_3cm	MCNP_3cm	MS_7.5cm	MCNP_7.5cm	MS_10cm	MCNP_10cm
E_γ = 3 MeV								
0	9.06E+03	9.29E+03	1.60E+03	1.74E+03	7.84E+01	8.92E+01	1.81E+01	2.08E+01
10	8.75E+03	8.94E+03	1.52E+03	1.65E+03	7.26E+01	8.16E+01	1.65E+01	1.87E+01
15	8.37E+03	8.55E+03	1.43E+03	1.55E+03	6.59E+01	7.38E+01	1.47E+01	1.66E+01
20	7.85E+03	8.02E+03	1.31E+03	1.42E+03	5.72E+01	6.43E+01	1.24E+01	1.40E+01
25	7.20E+03	7.34E+03	1.17E+03	1.27E+03	4.73E+01	5.32E+01	9.81E+00	1.11E+01
30	6.46E+03	6.59E+03	1.01E+03	1.09E+03	3.71E+01	4.17E+01	7.28E+00	8.24E+00
35	5.65E+03	5.76E+03	8.34E+02	9.07E+02	2.72E+01	3.06E+01	4.98E+00	5.63E+00
40	4.79E+03	4.88E+03	6.63E+02	7.20E+02	1.85E+01	2.07E+01	3.08E+00	3.49E+00
45	3.93E+03	4.01E+03	4.99E+02	5.41E+02	1.13E+01	1.27E+01	1.68E+00	1.91E+00
50	3.09E+03	3.14E+03	3.50E+02	3.79E+02	6.09E+00	6.88E+00	7.70E-01	8.88E-01
55	2.30E+03	2.33E+03	2.25E+02	2.42E+02	2.73E+00	3.12E+00	2.80E-01	3.31E-01
60	1.60E+03	1.60E+03	1.27E+02	1.36E+02	9.37E-01	1.11E+00	7.21E-02	9.08E-02
E_γ = 0.75 MeV								
0	2.04E+03	2.25E+03	1.26E+02	1.43E+02	4.82E-01	5.72E-01	2.63E-02	3.10E-02
10	1.95E+03	2.14E+03	1.17E+02	1.31E+02	4.18E-01	4.88E-01	2.19E-02	2.58E-02
15	1.85E+03	2.02E+03	1.06E+02	1.19E+02	3.48E-01	4.08E-01	1.73E-02	2.05E-02
20	1.71E+03	1.86E+03	9.29E+01	1.04E+02	2.67E-01	3.11E-01	1.23E-02	1.46E-02
25	1.54E+03	1.68E+03	7.75E+01	8.68E+01	1.86E-01	2.20E-01	7.80E-03	9.31E-03
30	1.35E+03	1.47E+03	6.13E+01	6.87E+01	1.17E-01	1.38E-01	4.29E-03	5.15E-03
35	1.14E+03	1.24E+03	4.56E+01	5.12E+01	6.43E-02	7.70E-02	2.00E-03	2.43E-03
40	9.27E+02	1.00E+03	3.14E+01	3.53E+01	3.02E-02	3.64E-02	7.54E-04	9.36E-04
45	7.19E+02	7.75E+02	1.97E+01	2.23E+01	1.15E-02	1.42E-02	2.18E-04	2.80E-04
50	5.26E+02	5.63E+02	1.09E+01	1.25E+01	3.34E-03	4.35E-03	4.38E-05	6.03E-05
55	3.55E+02	3.78E+02	5.08E+00	5.91E+00	6.59E-04	9.43E-04	5.33E-06	8.44E-06
60	2.15E+02	2.27E+02	1.85E+00	2.25E+00	7.37E-05	1.29E-04	3.08E-07	7.90E-07
E_γ = 0.3 MeV								
0	3.22E+01	3.71E+01	2.59E-03	2.99E-03	3.59E-12	3.93E-12	5.34E-17	5.43E-17
10	2.93E+01	3.31E+01	2.06E-03	2.35E-03	2.12E-12	2.34E-12	2.68E-17	2.74E-17
15	2.59E+01	2.93E+01	1.54E-03	1.76E-03	1.08E-12	1.21E-12	1.11E-17	1.16E-17
20	2.17E+01	2.46E+01	1.01E-03	1.16E-03	4.07E-13	4.67E-13	3.06E-18	3.34E-18
25	1.72E+01	1.95E+01	5.71E-04	6.70E-04	1.08E-13	1.31E-13	5.35E-19	6.29E-19
30	1.26E+01	1.44E+01	2.71E-04	3.24E-04	1.92E-14	2.45E-14	5.47E-20	7.29E-20
35	8.58E+00	9.81E+00	1.05E-04	1.29E-04	2.08E-15	3.19E-15	2.93E-21	5.53E-21
40	5.27E+00	6.06E+00	3.12E-05	4.14E-05	1.21E-16	3.31E-16	6.92E-23	6.57E-22
45	2.85E+00	3.32E+00	6.65E-06	9.95E-06	3.19E-18	4.36E-17	9.33E-25	2.56E-22
50	1.30E+00	1.56E+00	9.05E-07	1.77E-06	2.85E-20	1.79E-17	7.71E-25	1.32E-22
55	4.69E-01	5.95E-01	6.57E-08	2.57E-07	5.59E-23	1.26E-17	6.14E-25	6.95E-23
60	1.21E-01	1.75E-01	1.89E-09	4.78E-08	7.43E-25	8.31E-18	4.66E-25	3.79E-23

Appendix A.3:

Comparison of effective dose rates (mSv/hr) between MS and MCNP for iron.

α (deg.)	MS_1cm	MCNP_1cm	MS_3cm	MCNP_3cm	MS_7.5cm	MCNP_7.5cm	MS_10cm	MCNP_10cm
				E_γ = 3 MeV				
0	1.68E+03	1.81E+03	2.32E+02	2.49E+02	5.58E+00	5.98E+00	6.12E-01	6.67E-01
10	1.62E+03	1.73E+03	2.20E+02	2.33E+02	5.07E+00	5.40E+00	5.40E-01	5.80E-01
15	1.55E+03	1.65E+03	2.06E+02	2.17E+02	4.48E+00	4.80E+00	4.60E-01	4.93E-01
20	1.45E+03	1.55E+03	1.87E+02	1.97E+02	3.75E+00	4.03E+00	3.65E-01	3.91E-01
25	1.33E+03	1.42E+03	1.64E+02	1.72E+02	2.95E+00	3.15E+00	2.66E-01	2.87E-01
30	1.20E+03	1.27E+03	1.39E+02	1.46E+02	2.16E+00	2.31E+00	1.77E-01	1.92E-01
35	1.05E+03	1.11E+03	1.13E+02	1.18E+02	1.45E+00	1.56E+00	1.05E-01	1.13E-01
40	8.94E+02	9.38E+02	8.74E+01	9.04E+01	8.80E-01	9.42E-01	5.40E-02	5.87E-02
45	7.36E+02	7.66E+02	6.33E+01	6.53E+01	4.65E-01	5.05E-01	2.32E-02	2.58E-02
50	5.81E+02	5.97E+02	4.23E+01	4.33E+01	2.05E-01	2.27E-01	7.77E-03	8.93E-03
55	4.34E+02	4.39E+02	2.52E+01	2.57E+01	7.04E-02	8.17E-02	1.85E-03	2.31E-03
60	3.02E+02	2.99E+02	1.28E+01	1.31E+01	1.67E-02	2.19E-02	2.65E-04	4.03E-04
				E_γ = 0.75 MeV				
0	5.25E+02	5.53E+02	3.26E+01	3.31E+01	7.66E-02	8.00E-02	1.66E-03	1.74E-03
10	5.05E+02	5.31E+02	3.04E+01	3.04E+01	6.53E-02	6.82E-02	1.34E-03	1.43E-03
15	4.81E+02	5.04E+02	2.77E+01	2.76E+01	5.32E-02	5.60E-02	1.02E-03	1.09E-03
20	4.48E+02	4.67E+02	2.42E+01	2.40E+01	3.95E-02	4.20E-02	6.79E-04	7.39E-04
25	4.08E+02	4.22E+02	2.02E+01	2.00E+01	2.64E-02	2.84E-02	3.94E-04	4.36E-04
30	3.62E+02	3.70E+02	1.60E+01	1.58E+01	1.57E-02	1.71E-02	1.93E-04	2.21E-04
35	3.12E+02	3.15E+02	1.19E+01	1.17E+01	7.99E-03	9.12E-03	7.71E-05	9.30E-05
40	2.60E+02	2.58E+02	8.13E+00	8.07E+00	3.39E-03	4.14E-03	2.39E-05	3.19E-05
45	2.07E+02	2.02E+02	5.05E+00	5.07E+00	1.13E-03	1.57E-03	5.32E-06	8.11E-06
50	1.57E+02	1.49E+02	2.75E+00	2.86E+00	2.74E-04	4.81E-04	7.57E-07	1.94E-06
55	1.11E+02	1.02E+02	1.24E+00	1.39E+00	4.20E-05	1.33E-04	5.74E-08	4.18E-07
60	7.09E+01	6.25E+01	4.30E-01	5.78E-01	3.28E-06	3.57E-05	1.71E-09	1.13E-07
				E_γ = 0.3 MeV				
0	1.67E+02	1.66E+02	2.57E+00	2.59E+00	2.24E-04	2.58E-04	5.89E-07	7.28E-07
10	1.59E+02	1.58E+02	2.31E+00	2.31E+00	1.76E-04	2.02E-04	4.22E-07	5.28E-07
15	1.50E+02	1.48E+02	2.02E+00	2.02E+00	1.29E-04	1.51E-04	2.76E-07	3.50E-07
20	1.37E+02	1.35E+02	1.67E+00	1.67E+00	8.17E-05	9.87E-05	1.48E-07	1.96E-07
25	1.23E+02	1.20E+02	1.28E+00	1.30E+00	4.42E-05	5.58E-05	6.38E-08	8.98E-08
30	1.06E+02	1.02E+02	9.12E-01	9.39E-01	1.98E-05	2.68E-05	2.12E-08	3.32E-08
35	8.81E+01	8.38E+01	5.90E-01	6.24E-01	7.06E-06	1.10E-05	5.15E-09	9.64E-09
40	7.02E+01	6.58E+01	3.40E-01	3.78E-01	1.89E-06	3.70E-06	8.44E-10	2.25E-09
45	5.29E+01	4.88E+01	1.68E-01	2.05E-01	3.50E-07	1.07E-06	8.28E-11	4.74E-10
50	3.72E+01	3.36E+01	6.82E-02	9.83E-02	3.91E-08	2.90E-07	4.07E-12	1.29E-10
55	2.38E+01	2.12E+01	2.08E-02	4.09E-02	2.16E-09	9.16E-08	7.52E-14	4.88E-11
60	1.33E+01	1.18E+01	4.18E-03	1.53E-02	4.19E-11	3.24E-08	3.25E-16	1.62E-11

Appendix A.4:

Comparison of effective dose rates (mSv/hr) between MS and MCNP for concrete.

α (deg.)	MS_10cm	MCNP_10cm	MS_35cm	MCNP_35cm	MS_90cm	MCNP_90cm	MS_125cm	MCNP_125cm
				Eγ = 3 MeV				
0	5.86E+01	6.20E+01	4.61E+00	4.69E+00	2.48E-02	2.63E-02	9.98E-04	1.04E-03
10	5.64E+01	5.93E+01	4.32E+00	4.43E+00	2.17E-02	2.29E-02	8.33E-04	9.03E-04
15	5.37E+01	5.65E+01	3.97E+00	4.09E+00	1.82E-02	1.92E-02	6.60E-04	7.18E-04
20	5.02E+01	5.26E+01	3.51E+00	3.63E+00	1.42E-02	1.50E-02	4.71E-04	5.10E-04
25	4.58E+01	4.78E+01	2.98E+00	3.07E+00	1.01E-02	1.08E-02	2.99E-04	3.23E-04
30	4.08E+01	4.23E+01	2.42E+00	2.47E+00	6.47E-03	6.93E-03	1.65E-04	1.80E-04
35	3.53E+01	3.64E+01	1.85E+00	1.90E+00	3.67E-03	3.96E-03	7.68E-05	8.47E-05
40	2.96E+01	3.02E+01	1.32E+00	1.35E+00	1.78E-03	1.95E-03	2.90E-05	3.26E-05
45	2.38E+01	2.41E+01	8.67E-01	8.89E-01	7.09E-04	8.13E-04	8.37E-06	9.87E-06
50	1.83E+01	1.81E+01	5.06E-01	5.22E-01	2.16E-04	2.54E-04	1.68E-06	2.17E-06
55	1.31E+01	1.28E+01	2.53E-01	2.66E-01	4.54E-05	5.86E-05	2.01E-07	3.17E-07
60	8.62E+00	8.18E+00	1.00E-01	1.12E-01	5.49E-06	9.99E-06	1.13E-08	2.68E-08
				Eγ = 0.75 MeV				
0	1.74E+01	1.65E+01	3.28E-01	2.93E-01	3.04E-05	3.13E-05	7.65E-08	7.80E-08
10	1.67E+01	1.58E+01	2.97E-01	2.71E-01	2.38E-05	2.40E-05	5.47E-08	5.75E-08
15	1.57E+01	1.49E+01	2.60E-01	2.37E-01	1.74E-05	1.78E-05	3.55E-08	3.78E-08
20	1.45E+01	1.36E+01	2.15E-01	1.97E-01	1.10E-05	1.15E-05	1.90E-08	2.07E-08
25	1.30E+01	1.20E+01	1.67E-01	1.53E-01	5.95E-06	6.46E-06	8.10E-09	9.21E-09
30	1.13E+01	1.03E+01	1.19E-01	1.11E-01	2.65E-06	3.07E-06	2.66E-09	3.27E-09
35	9.53E+00	8.52E+00	7.80E-02	7.42E-02	9.39E-07	1.20E-06	6.34E-10	8.98E-10
40	7.68E+00	6.70E+00	4.53E-02	4.52E-02	2.49E-07	3.89E-07	1.01E-10	1.85E-10
45	5.87E+00	5.00E+00	2.26E-02	2.48E-02	4.52E-08	1.05E-07	9.56E-12	3.47E-11
50	4.20E+00	3.47E+00	9.21E-03	1.20E-02	4.95E-09	2.62E-08	4.47E-13	6.96E-12
55	2.73E+00	2.20E+00	2.82E-03	5.06E-03	2.63E-10	7.31E-09	7.72E-15	1.56E-12
60	1.56E+00	1.23E+00	5.69E-04	1.89E-03	4.80E-12	2.61E-09	3.03E-17	7.21E-13
				Eγ = 0.3 MeV				
0	6.50E+00	5.13E+00	2.59E-02	2.06E-02	4.64E-08	4.54E-08	8.61E-12	9.15E-12
10	6.18E+00	4.87E+00	2.26E-02	1.79E-02	3.28E-08	3.26E-08	5.32E-12	5.83E-12
15	5.78E+00	4.52E+00	1.89E-02	1.52E-02	2.10E-08	2.18E-08	2.87E-12	3.33E-12
20	5.26E+00	4.06E+00	1.46E-02	1.20E-02	1.10E-08	1.23E-08	1.17E-12	1.50E-12
25	4.63E+00	3.53E+00	1.02E-02	8.74E-03	4.56E-09	5.96E-09	3.44E-13	5.20E-13
30	3.92E+00	2.94E+00	6.47E-03	5.90E-03	1.44E-09	2.36E-09	6.94E-14	1.44E-13
35	3.18E+00	2.34E+00	3.59E-03	3.62E-03	3.28E-10	7.91E-10	8.84E-15	3.47E-14
40	2.45E+00	1.77E+00	1.69E-03	2.02E-03	4.91E-11	2.47E-10	6.31E-16	8.65E-15
45	1.76E+00	1.26E+00	6.46E-04	1.04E-03	4.28E-12	8.13E-11	2.10E-17	2.87E-15
50	1.16E+00	8.27E-01	1.85E-04	4.82E-04	1.79E-13	3.30E-11	2.47E-19	1.18E-15
55	6.73E-01	4.96E-01	3.55E-05	2.15E-04	2.64E-15	1.32E-11	6.62E-22	5.22E-16
60	3.29E-01	2.64E-01	3.75E-06	9.06E-05	8.19E-18	5.69E-12	3.57E-24	2.45E-16

Appendix A.5:

Relative deviation (%) between MS and MCNP for lead and iron.

		Lead				Iron		
α deg.)	**RD_1cm**	**RD_3cm**	**RD_7.5cm**	**RD_10cm**	RD_2cm	RD_7cm	RD_18cm	RD_25cm
				E_γ = 3 MeV				
0	-3	-9	-12	-13	-7	-7	-7	-8
10	-2	-8	-11	-12	-6	-5	-6	-7
15	-2	-8	-11	-12	-6	-5	-7	-7
20	-2	-8	-11	-12	-6	-5	-7	-7
25	-2	-8	-11	-12	-6	-5	-6	-7
30	-2	-8	-11	-12	-6	-4	-7	-8
35	-2	-8	-11	-12	-5	-4	-7	-7
40	-2	-8	-11	-12	-5	-3	-7	-8
45	-2	-8	-11	-12	-4	-3	-8	-10
50	-1	-8	-12	-13	-3	-2	-10	-13
55	-1	-7	-13	-15	-1	-2	-14	-20
60	0	-7	-16	-21	1	-3	-24	-34
				E_γ = 0.75 MeV				
0	-10	-12	-16	-15	-5	-2	-4	-4
10	-9	-11	-14	-15	-5	0	-4	-6
15	-9	-11	-15	-16	-5	0	-5	-7
20	-9	-11	-14	-16	-4	1	-6	-8
25	-8	-11	-15	-16	-3	1	-7	-10
30	-8	-11	-15	-17	-2	1	-8	-13
35	-8	-11	-16	-18	-1	1	-12	-17
40	-8	-11	-17	-19	1	1	-18	-25
45	-7	-12	-19	-22	3	0	-28	-34
50	-7	-13	-23	-27	5	-4	-43	-61
55	-6	-14	-30	-37	9	-11	-68	-86
60	-5	-18	-43	-61	13	-26	-91	-98
				E_γ = 0.3 MeV				
0	-13	-13	-9	-2	0	-1	-13	-19
10	-12	-12	-9	-2	1	0	-13	-20
15	-12	-12	-10	-5	1	0	-15	-21
20	-12	-13	-13	-8	2	0	-17	-24
25	-12	-15	-17	-15	3	-1	-21	-29
30	-12	-16	-22	-25	4	-3	-26	-36
35	-13	-19	-35	-47	5	-5	-36	-47
40	-13	-25	-63	-89	7	-10	-49	-63
45	-14	-33	-93	-100	8	-18	-67	-83
50	-17	-49	-100	-99	11	-31	-87	-97
55	-21	-74	-100	-99	12	-49	-98	-100
60	-31	-96	-100	-99	13	-73	-100	-100

Appendix A.6:

Relative deviation (%) between MS and MCNP for concrete.

α (deg.)	RD_10cm	RD_35cm	RD_90cm	RD_125cm
		E_γ = 3 MeV		
0	-6	-2	-6	-4
10	-5	-3	-5	-8
15	-5	-3	-5	-8
20	-5	-3	-6	-8
25	-4	-3	-6	-8
30	-4	-2	-7	-8
35	-3	-2	-7	-9
40	-2	-2	-9	-11
45	-1	-3	-13	-15
50	1	-3	-15	-23
55	3	-5	-22	-37
60	5	-11	-45	-58
		E_γ = 0.75 MeV		
0	5	12	-3	-2
10	5	9	-1	-5
15	6	10	-2	-6
20	7	9	-4	-8
25	8	9	-8	-12
30	10	7	-14	-19
35	12	5	-22	-29
40	15	0	-36	-45
45	17	-9	-57	-72
50	21	-23	-81	-94
55	24	-44	-96	-100
60	26	-70	-100	-100
		E_γ = 0.3 MeV		
0	27	26	2	-6
10	27	26	0	-9
15	28	24	-4	-14
20	29	21	-11	-22
25	31	17	-23	-34
30	33	10	-39	-52
35	36	-1	-59	-75
40	38	-16	-80	-93
45	40	-38	-95	-99
50	40	-62	-99	-100
55	36	-84	-100	-100
60	25	-96	-100	-100

References

[1] MicroShield 5.05, *Grove Engineering*, FRAMATOME, ANP, USA, 1992-2000.

[2] Oliveira, A. D. and Oliveira, C., *Comparison of Deterministic and Monte Carlo Methods in Shielding Design.*, Rad. Prot. Dosimetry, Vol, 115, No. 1-4,pp. 254-257, 2005.

[3] X-5 Monte Carlo Team, *MCNP-A General Monte Carlo N-Particle Transport Code, version 5. Los Alamos National Laboratory*, USA, April 24, 2003.

[4] DeMarco J. J. Boederker K. and Wallace R. E., *An Analysis of MCNP cross-sections and tally methods for low-energy photons.* Phys. Med. Biol., 47, 1321-1332, 2002.

[5] Negin, C. A., and Worku, G., *MicroShield 6 Verification and Validation.* Grove Engineering, Inc, 1992.

[6] Malefant, R. E., *QAD: A Series of Point-Kernel General-Purpose Shielding Programs.* Rep. No. LA-3473, Los Alamos Scientific Lab, Apr. 1967.

[7] John, A., Peoples and Daniel Fieno., *Transport Study of Neutron and Photon Attenuation Through Lithium Hydride AND Tungstan Spherical Media.* National Aeronautics And Space Administration. Washington, D. C., 1969.

[8] Jaeger, R. G, *Engineering Compendium on Radiation Shielding Materials,* Springer-Verlag, New York, Vol. II, 1975.

[9] Shultis, J. K and Faw, R. E, *Principles of radiation shielding,* 2000.

[10] Leo, W. R, *Techniques for Nuclear and Particle Physics Experiments,* Springer-Verlag, 1994.

[11] Lamarsh, W. R and Baratta, A. J, *Introduction to Nuclear Engineering,* 3rd Ed, 2001.

[12] Johns, H. E, Cunningghan, J. R, *The Physics of Radiology,* 4th Ed, 1983.

[13] Burcham, W. E., *Nuclear Physics — an Introductio,* 2nd Long Group Ltd, 1973.

[14] Mukhin, K. N., *Nuclear Physics,* Macdonald Technical and Scientic London, 1970.

[15] Hubbell, J. H, *Photon Mass Attenuation and Energy Absorption Coefficients from 1 KeV to 20 MeV,* Int. Jour. Appl. Rad. Isot. 33, 1982.

[16] Knoll, G. F, *Radiation Detection and Measurements,* 3rd Ed. 2000.

[17] Evans, R. D, *Atomic Nucleus,* McGraw-Hill NY, 1955.

[18] Meitner, L. and Hupfeld, H. H., *Naturwiss,* 18, 534-535, 1949.

[19] Hofstadter, R. and McIntyre, J. A., *Phys. Rev.*, 76, 1269-1270, 1949.

[20] Cross, W. G. and Ramsay, N. F., *Phys. Rev.*, 80, 929-936, 1950.

[21] Shultis, J. K and Faw, F. E., *Health Phys.*, 88(4): 297-322; 2005.

[22] Shumizu, A., *Calculation of Gamma-Ray Build-Up Factors up to Depths of 100 mfp by the Method of Invariance Embedding, (I) Analysis of Accurancy and Comparison with other Data.*, J. Nucl. Sc. and Tech., Vol. 39, No. 5, pp. 477-486, May 2002.

[23] Malefant, M. P., *QAD: A series of point kernel general-purpose shielding programs,* Los Alamos National Laboratory LA-3573, 1967.

[24] Cain, V.R., *A users manual for QAD-CG, the combinational geometry version of the QAD-P5A point kernel shielding code*, San Francisco, CA: Bechtel Power Corp., Report, NE007, 1977.

[25] Price, J. H. and Blattner, W. G. M., *Utilization instructions for QADMOD-G. Fort Worth, TX: Radiation Research Assoc., Inc., Available from RSCC as CCC565/QADMOD-GP.*, RRA-N7914, 1979.

[26] Malefant, R. E., *G3: A general purpose gamma-ray scattering code*, Los Alamos, NM: Los Alamos National Laboratory; Available from RSICC as CCC-564/G33-GP, LA-5176, 1973.

[27] Goldstein, H. and Wilkins, J. E., *NY: Nuclear Development Associates.*, NYO-3075, 1954.

[28] American Nuclear Standards, *Gamma-Ray Attenuation Coefficients and Buildup Factors for engineering Materials.*, ANSI/ANS-6.4.3, 1991.

[29] Takeuchi, K. and Tanaka, S., *PALLAS-1D (VII).*, JAERI-M84-214, 1984.

[30] Taylor, J. J., *Washington DC: Westinghouse Electric Corporation, Atomic Power Division,* USAEC Report WAPD-RM-217, 1954.

[31] Berger, M. J. and Doggert, J. A., *Semi-analytic Monte Carlo calculation,* J. Res. Nat., Bur Stand 56:89-98, 1956.

[32] Capo, M. A. *Washington DC: Westinghouse Electric Corporation, Atomic Power Division.* USAEC Report APEX-510, 1959.

[33] Spanier, J. and Gelbard, E. M., *Monte Carlo Principles and Neutron Transport Problems,* Addison-Weshley Pub. Cop., 1969.

[34] Dubi, A., *Monte Carlo Calculations for Nuclear Reactors,* CRC Handbook of Nuclear Reactor Calculations, Volume II. CRC Press, Inc, Boca Raton, Florida, USA, 1986.

[35] Reynaert, N., Van der Marck S. C., Schaart, D. R., Van der Zee, W., Van Vliet-Vroegindeweij, C., Tomsej, J., Heijmen, B., Coghe, M., de Wagter, C., Rad. Phys.and Chem. 76, 643-686, 2007.

[36] ICRP Publication, *Data for use in Protection Against External Radiation.* The International Commission on Radiological Protection, 1987.

[37] Carter, L. L. and Cashwell, E. D., *Particle Transport Simulations with Monte Carlo Method,* ERDA Critical Review Series, TID-26607, 1975.

[38] Haghighat, A. and Wagner, J. C., *Monte Carlo Variance Reduction with Deterministic Importance functions,* Progress in Nuclear Energy, 42 25-53, 2003.

[39] Lux, I. and L. Koblinger., *Monte Carlo Particle Transport Methods: Neutron and Photon Calculations,* CRC Press, Boca Raton, FL, 1990.